2007-01-02

# High-Frequency Ultrasound Drug Delivery and Cavitation

Mario Alfonso Diaz
*Brigham Young University - Provo*

# HIGH-FREQUENCY ULTRASOUND DRUG DELIVERY AND CAVITATION

by

Mario Alfonso Díaz de la Rosa

A thesis submitted to the faculty of

Brigham Young University

in partial fulfillment of the requirements for the degree of

Master of Science

Department Chemical Engineering

Brigham Young University

April 2007

BRIGHAM YOUNG UNIVERSITY

GRADUATE COMMITTEE APPROVAL

of a thesis submitted by

Mario Alfonso Díaz de la Rosa

This thesis has been read by each member of the following graduate committee and by majority vote has been found to be satisfactory.

| | |
|---|---|
| Date | William G. Pitt, Chair |
| Date | Ghaleb A. Husseini |
| Date | Hugh B. Hales |

BRIGHAM YOUNG UNIVERSITY

As chair of the candidate's graduate committee, I have read the thesis of Mario Alfonso Díaz de la Rosa in its final form and have found that (1) its format, citations, and bibliographical style are consistent and acceptable and fulfill university and department style requirements; (2) its illustrative materials including figures, tables, and charts are in place; and (3) the final manuscript is satisfactory to the graduate committee and is ready for submission to the university library.

Date

William G. Pitt
Chair, Graduate Committee

Accepted for the Department

Larry L. Baxter
Graduate Coordinator

Accepted for the College

Alan R. Parkinson
Dean, Ira A. Fulton College of
Engineering and Technology

ABSTRACT

HIGH-FREQUENCY ULTRASOUND DRUG DELIVERY

AND CAVITATION

Mario Alfonso Díaz de la Rosa

Department Chemical Engineering

Master of Science

The viability of a drug delivery system which encapsulates chemotherapeutic drugs (Doxorubicin) in the hydrophobic core of polymeric micelles and triggers release by ultrasound application was investigated at an applied frequency of 500 kHz. The investigation also included elucidating the mechanism of drug release at 70 kHz, a frequency which had previously been shown to induce drug release.

A fluorescence detection chamber was used to measure *in vitro* drug release from both Pluronic$^{TM}$ and stabilized micelles and a hydrophone was used to monitor bubble activity during the experiments. A threshold for release between 0.35 and 0.40 in mechanical index was found at 70 kHz and shown to correspond with the appearance of the subharmonic signal in the acoustic spectrum. Additionally, drug release was found to correlate with increase in subharmonic emission. No evidence of drug release or of the subharmonic signal was detected at 500 kHz. These findings confirmed the role of cavitation in ultrasonic drug release from micelles.

A mathematical model of a bubble oscillator was solved to explore the differences in the behavior of a single 10 $\mu$m bubble under 70 and 500 kHz ultrasound. The dynamics were found to be fundamentally different; the bubble follows a period-doubling route to chaos at 500 kHz and an intermittent route to chaos at 70 kHz. It was concluded that this type of "intermittent subharmonic" oscillation is associated with the apparent drug release.

This research confirmed the central role of cavitation in ultrasonically-triggered drug delivery from micelles, established the importance of subharmonic bubble oscillations as an indicator, and expounded the key dynamic differences between 70 and 500 kHz ultrasonic cavitation.

# ACKNOWLEDGMENTS

In the process of completing this endeavor I have been blessed with the invaluable help and support of friends and family. The following is a list (incomplete, I am sure) of those whose contributions to this work cannot, must not, go unmentioned.

I was fortunate to have Dr. William Pitt as a mentor, teacher, friend, and all-around putative father during both my undergraduate and graduate work. His instruction and example define what makes a great advisor; none of this would be possible without his guidance. His former student and present collaborator Dr. Ghaleb Husseini paved the way for this work and was there with me almost every step of the way. I have learned a great deal from his experience and expertise and I will be forever grateful for his friendship and professional advice. Thank you Ghaleb, this work is as much yours as it is mine. Thanks must also be extended to Dr. Douglas Christensen at the University of Utah for providing the laser detection system, a lab in which to work long nights, and great insight and instruction.

A number of great friends kept me sane as this project, school, and Provo ravaged my soul. Christopher Cornwell, Gretchen Rimmasch, and Rissie Lundberg are all fellow graduate students and lifelong friends who were always a short walk away and willing to give of themselves at a moment's notice. Gregory Gardner shared in the trying undergraduate experience and has given me his friendship and support ever since. I would like to thank Ben Jepson for being such an understanding roommate and friend. Nick Grant, for the many lunches and long discussions, thank you. Jenn Rose and Lynda Varela I would like to thank for their unconditional friendship and the many concerts we have shared together.

Working in Dr. Pitt's lab meant interacting with great students who helped move this project along through both discussion and, sometimes, direct help. I would like to specifically thank Dr. Zeng Yi, Dr. Hua Lei, Michael Parini, Eric Richardson, Timothy Pickett, and Travis Fixmer. Tim Miller, Phil Smith, Brian Critchfield, and Aaron Nackos shared in the pains of being a graduate student: thanks, guys.

Ultimately, it is my family to whom I am most indebted. My sister Luz, her husband Jorge Robles, and their beautiful daughter Aileen gave me a home away from home. My sister's love and support through the years can never be repaid. Above all, I would like to thank my parents, Juan Alfonso Díaz and Luz Maria de la Rosa. I could write volumes on how much I owe them for any and all of my successes but they would all undoubtedly be insufficient to accurately reflect their contributions. For your example, teaching, support, understanding, sacrifice, and love, thank you so much, mom and dad. Anything good that I am, I owe it to you.

# Table of Contents

## List of Figures

# Chapter 1

# Introduction

The therapeutic treatment of localized ailments (such as cancer) requiring a potent and harmful drug that can only be administered systemically is best served by the development of a system that is able to control the delivery of the drug in both space (the afflicted area) and time (activation/deactivation of treatment). One such modality that shows promise both of these areas employs sequestering vesicles to encapsulate the drug and prevent its interaction with healthy tissue; these capsules are eventually induced to release their contents at the site of interest via the application of an external trigger. Hence, the optimization of the drug delivery problem necessitates the development of both an effective, stable, biodegradable carrier and an external system that is able to activate the carrier in a safe and controllable manner.

Research by Husseini and others [26, 27, 28, 29] has shown that the combination of polymeric micelles and ultrasound (US) constitutes a promising drug delivery system. In particular, they showed that micelles of the triblock copolymer Pluronic P105 (PEO-PPO-PEO) are able to release anthracycline agents within their hydrophobic core upon application of low-frequency ultrasound. Furthermore, *in vivo* studies with a rat tumor model [61] showed that the activity of the chemotherapy agent Doxorubicin (Dox) is enhanced by US application: the size of the targeted tumor in a leg was significantly reduced in comparison with the non-targeted tumor in the opposite leg. Finally, in the same lab, Pruitt *et al.* [77] showed that the Pluronic carriers can be further stabilized in order to increase their circulation time in the body.

At this point the attention turns to the best possible use of US in the system described above. Ultrasonic waves (pressure waves with frequencies greater than 20

kHz) can be focused, reflected and refracted, and propagated through a medium, hence their appeal as a targeting modality for drug delivery. That US is such an attractive tool is evident considering its non-invasive nature, its ubiquity as a diagnostic tool which in turn has generated an advanced field of US instrumentation, and the ability to focus and control insonation in practice. The latter, however, is generally achieved at frequencies higher than those studied in the research discussed above for at least two important rules of thumb of US instrumentation: US cannot be focused to a volume of less than half a wavelength in diameter and a focused transducer must be at least about ten wavelengths in diameter. Hence, as frequency decreases and wavelength increases, focusing becomes more problematic and impractical. It is therefore imperative to investigate the system's efficacy at higher frequencies. This is a critical question, for it is speculated that the underlying physical mechanism of release is partly due to a phenomenon known as cavitation, which is defined as the formation and/or activity of gas or vapor-filled cavities in a medium exposed to an acoustic field [9]. Furthermore, it may be the case that the high forces associated with eventual bubble collapse (known as inertial or collapse cavitation) are needed to achieve release. Such cavitation activity, however, has been shown to exhibit a threshold which increases with increasing US frequency.

Confirmation of the system's ability to release drug in a controlled manner at frequencies near the diagnostic level will eventually allow for the implementation of a clinical US device that releases drug in the desired location of treatment through focused insonation. This research sought to establish, from both an experimental and theoretical point of view, whether the polymeric carrier system developed by Pitt *et al.* is able to release drug at frequencies (such as 500 kHz) which are close to the levels used in the well-established field of US diagnostics.

# Chapter 2

# Literature Review

The literature background for this research can be divided into three separate categories: the study of polymeric drug delivery carriers, the use of ultrasound as a drug delivery tool, and the physics of bubble dynamics (in particular, cavitation phenomena). The synthesis of these categories allows one to understand the physics of interaction between micellar carriers and ultrasound, which was integral to the goals of this project.

## 2.1 Polymeric Carriers for Drug Delivery

Research in drug delivery carriers has mainly focused on the study of liposomes. Liposomes are much larger than micelles ($\sim 1\mu m$ vs. $\sim 0.05\mu m$), are more difficult to prepare, and are used, for the most part, to encase the drug in order to prevent any release [18]. Nevertheless, several investigators have used ultrasound to disrupt drug-loaded liposomes and release their contents [63, 91, 94]; yet it is important to mention that this release is irreversible: once released, the liposomes are unable to re-encapsulate their contents.

The study of polymeric micelles as drug delivery vehicles has revealed a number of advantages over other types [97], including 1) structural stability, or slow dissolution levels below their critical micelle concentration (CMC), which is the concentration at which micelles form at a given temperature [35]; 2) prolonged shelf life; 3) long circulation time in blood and stability in biological fluids; 4) an appropriately large size to prevent renal excretion and yet 5) small enough to allow extravasation at the tumor site; 6) simplicity in drug incorporation (no need for covalent bonding to the carrier); and 7) drug delivery independent of drug character [79].

The micelles formed by Pluronic$^{TM}$, which is a triblock copolymer of poly(ethylene oxide) (PEO) and poly(propylene oxide) (PPO) and denoted as PEO-PPO-PEO, have been studied as potential vehicles for drug delivery. These micelles are especially attractive for cancer drug delivery since their polyethylene glycol shell chains prevent clearance by cells of the reticuloendothelial system (thus ensuring appropriate circulation times) and they have been shown to sensitize multi-drug resistant (MDR) cancer cells [8] and to have low toxicity [7] .

Rapoport *et al.* found that Pluronic$^{TM}$ P105 was an ideal carrier among the family of Pluronics$^{TM}$ as it 1) quickly forms micelles upon simple dissolution in water; 2) its PPO core is sufficiently hydrophobic to stabilize the micelle and sequester hydrophobic drugs [60]; 3) the micelles can be perturbed by low frequency ultrasound to release the drug [27]; 4) the drug is quickly re-encapsulated in the carrier when insonation is stopped [28]; and 5) Pluronic$^{TM}$ at low concentrations is non-toxic and can be cleared by the kidneys [93]. Other types of Pluronics$^{TM}$ (P85, L61, and F108) were discarded as candidates since those with longer PEO blocks had too high of a CMC and those with longer PPO blocks could not dissolve easily in water [76].

Pruitt *et al.* developed a stable form of the P105 carrier that would not dissolve upon I.V. injection and instantly release their contents into the blood [76]. This premature release invariably occurred when P105 was used *in vivo* as the micelles were diluted below their CMC. Work by Pruitt created a stabilized micelle called Plurogel$^{TM}$ by polymerizing an interpenetrating network of thermally sensitive *N*,*N*-diethyl acrylamide (pNNDEA) in the hydrophobic core of P105 using bis-acryloyl cystamine (BAC) as the crosslinker [77]. The carriers were shown to sequester and release Dox upon insonation (albeit less than Pluronic$^{TM}$ micelles released) [26] and to be biodegradable as shown by using diphenyl hexatriene as a fluorescent probe to track the temporal stability of its hydrophobic environment [76].

Recently, Zeng *et al.* developed a stabilized micelle carrier called PNHL [98]. The micelle-forming polymer in PNHL consists of a block of PEO adjacent to a random copolymer of *N*-isopropyl acrylamide (NIPAAm) and polylactate esters of hydroxy-ethyl methacrylate (HEMA-lactate). By means of the PEO shell, PNHL re-

tains the stealth characteristics of the carriers already described, while the hydrophobic core provides the stable hydrophobic environment of Plurogel$^{TM}$. The advantage lies in the biodegradability of the NIPAAm-HEMA-lactate block: the relative composition of these three compounds controls the lifetime of the polymer, giving PNHL a greater flexibility of design as a drug carrier over Plurogel$^{TM}$.

## 2.2 Ultrasound and Drug Delivery

Generally speaking, research into US-mediated biological phenomena has focused on two categories: thermal and non-thermal effects. The former refers to the absorption of acoustic energy by fluids and tissues while the latter is normally associated with bubble oscillations (cavitation) [64]. Prior research has mostly emphasized these non-thermal phenomena since cavitation bio-effects lead to significant stresses on cells, facilitating transport of drugs and other molecules into the cytoplasm. While combinatorial and synergistic effects have not been ruled out, mechanistic questions have mostly centered on the role of cavitation in observed bio-effects, specifically as to the question of sonoporation (the production of transient holes in the cell membrane).

In the literature, when evidence points to membrane perturbation by US, the question turns to the kind of cavitation responsible for the effect. Cavitation can be divided into two types: stable and inertial (or collapse). Stable cavitation refers simply to the repeated oscillation of bubble diameter without collapse which is common at lower acoustic intensities. Inertial cavitation occurs when the acoustic pressure increases to a level where the oscillations become nonlinear and are violent enough that the inertia of the inward moving water overcomes the internal pressure of the bubble, causing the bubble to collapse. Inertial cavitation occurs readily as the bubble approaches its resonance size). This collapse is strong enough to produce shock waves, high temperatures and pressures, and free radicals [64]. Detection of these phenomena is accomplished by several methods, including measurement of the acoustic spectra generated by the bubble oscillations, trapping of free radicals, sonoluminescence, and effect inhibition as ambient pressure is increased [4, 13, 16, 59]. Of particular interest are the acoustic signals generated by the cavitating bubbles: for

a given driving frequency $f$, stable cavitation has been linked to the generation of harmonic ($nf, n \in \mathbb{N}$) and subharmonic ($f/2$) frequencies [9, 48, 51], while collapse cavitation has been associated with an increase in the non-harmonic background noise (shock wave-produced broadband emission) and with the subharmonic signal as well [20, 21, 31, 62]. Curiously, the subharmonic signal has been found indicative of both types of cavitation and the literature is conflicting in its conclusions; to this day, the subharmonic remains an enigma. Regardless, these are the phenomena that accompany any discussion of the mechanisms behind ultrasonic bio-effects.

One important application that has been studied is transdermal drug delivery; early research showed limited drug transport with treatment at the higher, diagnostic frequencies [34, 54]. Later studies by Mitragotri at 20 kHz revealed that US can deliver large and polar biomolecules such as insulin, interferon, and erythropoeitin across the stratum corneum [53]. More importantly, these studies presented evidence that collapse cavitation was responsible for skin permeability, including an inverse dependence on frequency and a threshold for the observed effect [41, 53, 55, 56, 57, 90]. The existence of a threshold for the onset of collapse cavitation is well established in literature [9, 12, 17, 21, 40, 92]. A classic study by Hill revealed thresholds for inertial cavitation to be near 1 W/cm$^2$ from 0.25 to 4 MHz by correlation with iodine release and the subharmonic signal [21]. Collapse cavitation thresholds between 0.036 and 0.141 W/cm$^2$ for 750 kHz US were reported by Daniels *et al.* Other studies have reported the dependence of the threshold for inertial cavitation on frequency and bubble size [17, 3]. Thresholds for bio-effects have also been found, but these vary with the type of cell or tissue being studied [5, 21, 25, 30, 52, 56, 58, 64, 82, 88, 90].

Cell membrane permeabilization by US has been observed in bovine corneal endothelial cells (20 kHz) [83], human leukemia (HL-60) cells (255 kHz) [89], and in embryonic chick 3T3 fibroblasts (1 MHz) [87]. Increased permeability of angiogenic blood vessels in the presence of stable liposomes has also been observed under the action of high frequency US [39]. In addition, Rapoport *et al.* demonstrated that 80 kHz US is able to permeabilize the cell wall of *Pseudomonas aeruginosa* [80], and, furthermore, reported that such phenomenon is accompanied by a threshold [95].

Husseini *et al.* have reported similar observations pertaining to the system in question in this thesis. Using a laser fluorescence detection system they quantitated the amount and kinetics of Dox release from P105 micelles [27] exposed to 20 and 70 kHz US. Since Dox molecules absorb light at 488 nm and isotropically emit fluorescence light between 530 and 630 nm, a fiber optic probe was used to collect the emission from the sample. Dox fluorescence is quenched when its surrounding environment changes from hydrophobic to hydrophilic, and hence a decrease in fluorescence was attributed to the release of Dox from the micelle core to the aqueous phase. The percent release of Dox from the micelles was then calculated after calibration with free (no micelles) Dox. It was found that P105 micelles released up to 10 % of their Dox load upon application of US, followed by complete re-encapsulation when US was turned off [27, 28].

Husseini *et al.* have also reported that the amount of Dox release from Pluronic$^{TM}$ micelles increases with increasing ultrasonic intensity and decreases with the driving frequency [26, 28]. This is significant since it is consistent with a cavitation mechanism (bubble amplitude and cavitation activity increases as frequency decreases). In the same study, they also showed that release decreased in a nearly linear manner with decreasing intensity, suggesting a low threshold for release (although no data were presented for intensities very near 0 W/cm$^2$).

The same group performed *in vitro* work with HL-60 cancer cells by exposing them to 70 kHz US in the presence of Dox and Dox encapsulated in either Pluronic$^{TM}$ or Plurogel$^{TM}$ micelles [29, 78]. They reported that the carriers prevented interactions with leukemia cells, increasing cell survival compared to free Dox. More surprisingly, they also discovered a synergistic lethal effect between US, DOX and the micellar carriers.

A rat model of colon cancer was used by Nelson *et al.* to test the system *in vivo* by inoculating BDIX rats in each hind leg with a suspension of DHD/K12/TRb colorectal cancer cells and subsequently exposing them to either 20 or 70 kHz US after systemic administration of free or encapsulated Dox [61]. Measurement of normalized

tumor volume after six weeks of treatment revealed that US-treated tumors generally slowed in growth compared to non-insonated tumors and in some cases even regressed.

### 2.3 Bubble Dynamics

Any discussion on bubble dynamics must invariably begin with the classic Rayleigh-Plesset equation [9, 64], which is a basic form of the momentum conservation equation. It assumes a spherical, isolated, internally homogeneous bubble in an infinite liquid medium in the absence of thermal and mass transfer effects. The medium is assumed to be unchanging as well. Due to these limitations, a number of modifications were made to the original model in order to account for the thermodynamic and transport-related complexities ignored in the first formulation. Modifications have included (but are not limited to): (1) the assumption of polytropic gas behavior by Noltingk, Neppiras, and Poritsky, (2) the addition of liquid compressibility effects by Keller and Kolodner [9], and (3) the myriad formulations of Prosperetti [32, 73, 74, 75] which aimed to include heat and mass transfer effects (see also Church [10, 11]). Brennen [9] provides a detailed overview of these developments.

The available literature is not limited to the study of single oscillating bubbles. A number of models for bubble clouds or clusters have been developed [1, 50, 65] that show that the energy generated by the oscillations of the cluster tends to concentrate in the center bubble. The phenomenon known as sonoluminescence (light emission by collapsing bubbles in water associated with cavitation activity) has been modeled by incorporating the momentum equation with a kinetic model of the radical reaction involved [33, 38]. The behavior of bubbles under the action of lithotripter shock waves has also been modeled, integrating the effects of bubble coatings and surrounding tissues or vessels [15].

In general, the results derived from the models described above tend to reproduce experimental findings reasonably well, with model-experiment agreement improving with increasing model complexity, as expected [9]. In particular, several well-known signatures of bubble behavior under the influence of an acoustic field have been reproduced with some measure of success, including: (1) thresholds and windows

for shape instability and growth by rectified diffusion [10, 96], (2) radial oscillation paths to sonoluminescence [19], and, of course, (3) subharmonic emission thresholds [32, 38, 42, 46, 47, 50, 67, 68, 70, 71, 72, 84].

Despite its relative lack of sophistication, however, the Rayleigh-Plesset equation (more precisely, the Noltingk/Neppiras/Poritsky modification of the original equation) contains enough nonlinearities to make its analysis a complicated task. In fact, the Rayleigh-Plesset equation is an example of what is called a *chaotic dynamical system* [46]. Among all who have studied the dynamics of these models from a dynamical systems perspective, Lauterborn has produced the definitive work [42, 43, 44, 45], including two comprehensive reviews [46, 67]. Prosperetti, while contributing mostly to the development of more mathematically rigorous and physically accurate models and numerical analysis techniques [74, 75], has also approached the study of bubble dynamics from this point of view [32, 70].

Lauterborn was the first [43] to report that the acoustic spectrum of cavitating bubbles approached an increased background noise (which he defined as chaos) through successive appearances of half-harmonics of the driving frequency (22.56 kHz). This was the first experiment to physically show the famous *period-doubling route to chaos* predicted by dynamical systems theory [14], and which is characteristic of driven nonlinear oscillators. Lauterborn proceeded to cement his findings by numerically repeating the phenomenon using a modification of the Gilmore model (which introduces an enthalpic term into the equation) for a frequency of 23.56 kHz [47]. For this study, Lauterborn created orbit diagrams clearly showing the period-doubling cascade at a fixed equilibrium bubble size of 230 $\mu$m across a range of 0 to 10 bar. Lauterborn gave further evidence that the acoustic signals of cavitating bubbles trace a deterministically chaotic system by calculating the largest Liapunov exponent from a time series of experimental values taken at a frequency of 22.9 kHz. It was found that the exponent converged to a value of 1.9, thus showing that the system exhibits sensitive dependence on initial conditions [24]. In an introductory review of the basic tools of chaos theory [46], Lauterborn shows the development of a period-doubling route to chaos for a bubble of radius 10 $\mu$m with a fixed pressure of

90 kPa and the driving frequency as a parameter (the appearance of the subharmonic occurring at 197 kHz).

In Lauterborn's most comprehensive exposition on bubble dynamics [67], he takes on the task of describing the bifurcation structure of bubble oscillators in a large section of parameter space. The model used was a modification of Properetti's own modification of the Keller and Miksis model and was not integrated directly in order to reduce the numerical load. A topologically equivalent system was solved instead and then transformed back to the space of interest by means of a diffeomorphism. All calculations were made for an equilibrium radius of 10 $\mu$m while the frequency varied anywhere from 30 kHz to 1 MHz. Lauterborn's approach was exhaustive, producing bifurcation diagrams, orbit diagrams, Poincaré maps, and plots of the basins of attraction for a number of parameters. His results showed the immensely rich dynamics inherent in the nonlinearities of the bubble oscillators, producing quite different results for different parameter values (thereby implying that all one can see is but a small section of a vast, truly complicated space). His analysis, however, lacked any useful results on the bifurcation structure as it relates to changes in driving pressure amplitude since he limited his calculations to changes in driving frequency. This is unfortunate since most experimental protocols call for a variation in applied pressure rather than driving frequency.

Lauterborn has also captured visual images of bubble collapse and jet formation [45] by means of high-speed photography. More significantly, he has provided holographic evidence of period-doubling in a bubble undergoing cavitation and eventual collapse [44].

Kim *et al.* reported that the pressure dependent (from about 1 to 1.4 atm pressure amplitude) bifurcation behavior for a 5 $\mu$m bubble at 28.84 kHz is not period-doubling but rather a "selective"' one [38], further demonstrating the need for a clear investigation of the dynamics induced by pressure variations. Finally, Phelps and Leighton [68] showed that there exists a repeatable onset of subharmonic emission for bubbles of various resonant frequencies and considered three possible mechanisms for the appearance of the subharmonic: (1) a period-doubling bifurcation, (2) the

presence of bubbles with an equilibrium radius twice the size of the one resonant with the driving field, and (3) surface waves. Surprisingly, theoretical examination of cases (1) and (2) yielded thresholds four to three orders of magnitude higher than experimental results, leading them to conclude that (3) was responsible (out of harmony with Leighton's own theory [48] that the subharmonic is the result of a prolonged expansion phase by the bubble preceding its collapse).

# Chapter 3

# Objectives

The individual objectives of this thesis were to:

1. Investigate drug release from micelles under the action of a 500 kHz, focused ultrasonic transducer. This was done by modifying the fluorescence detection system used previously [27] in order to capture fluorescence emission from a small volume by means of a bifurcated fiber optic bundle containing fibers used for both Dox excitation and fluorescence collection.

2. Search for evidence of cavitation during drug release from micelles at 70 kHz and 500 kHz. This was done in two ways: by carrying out *in vitro* drug release experiments at 70 and 500 kHz and measuring release of drug within the previously unexplored narrow window of 0-1 W/cm$^2$ in order to find a threshold for release (if any) and by using a calibrated hydrophone to monitor the acoustic signals emitted by the oscillating bubbles and tracking:

    - subharmonic and ultraharmonic signals
    - background noise emission
    - any apparent thresholds for acoustic signals

3. Mathematically model the bubble dynamics of the system with the purpose of elucidating the mechanism underlying drug release. Specifically, the models were used to reproduce the cavitation signals encountered in (2) and to subsequently relate the observed behavior of the system to physical arguments established in the literature.

# Chapter 4

# Materials and Methods

## 4.1 Drug Release Experiments

### 4.1.1 Fluorescence Detection

Preparation of the drug micelle carriers followed the protocol already established by Husseini *et al.* [27]: a Pluronic$^{TM}$ P105 (BASF, Mount Olive, NJ) solution (10 wt% in PBS) was loaded with 10 $\mu$g/mL Dox (a control of Dox at this concentration in pure PBS was also prepared). Stabilized Plurogel$^{TM}$ [77] and PNHL [98] were synthesized by Yi Zeng and similarly loaded with 10 $\mu$g/mL Dox.

The apparatus previously used to measure drug release [27] was modified in order to capture fluorescence emission from a small volume. A branch of a bifurcated fiber optic bundle directed a 488 nm beam of an argon ion laser (Ion Laser Technology, 5500 A) into a transparent (both optically and acoustically) plastic tube of cellulose butyrate containing the drug solution. Dox molecules absorbed the light at 488 nm and emitted fluorescent light between 530 and 630 nm. This emitted fluorescence was then captured by fibers in the fiber optic bundle and directed through its second branch to a silicon detector (EG&G 450-1). A dielectric bandpass filter (Omega Optical 535DF35) was used to eliminate emissions below 517 nm and above 552 nm. Finally, the signal from the photodetector was captured on an oscilloscope (Tektronix TDS 3012) and stored.

The amount of drug release from the micelles was calculated from the data acquired by the system described above by using the same analysis as Husseini *et al.* [27]. It was assumed that the decrease in fluorescence of the solution was proportional to the amount of drug released relative to a known baseline. Dox fluorescence at 100

% release was approximated by the measured fluorescence of Dox in PBS ($I_{PBS}$) while the Dox fluorescence at 0 % release was approximated by the measured fluorescence of Dox in the carrier without the action of US ($I_{P105}$). Hence, the percent drug release was defined as

$$\% \text{ release} = \frac{I_{P105} - I_{US}}{I_{P105} - I_{PBS}} \times 100\%, \tag{4.1}$$

where $I_{US}$ is the fluorescence intensity under the action of US.

### 4.1.2 Ultrasonic Insonation

An ultrasonicating bath (SC-40, Sonicor, Copiaque, NY)) filled with degassed water was used to apply US at 70 kHz, as was done in previous work [27]. A calibrated hydrophone (Bruel and Kjaer 8103, Decatur, GA) was used to find an acoustically intense spot wherein the Dox solution and the end of the fiber optic bundle were placed. A variable AC transformer was used to power the bath and to produce a range of intensities of ultrasound from 0 to 1 W/cm$^2$. The fluorescence and acoustic measurements at each intensity level were repeated at least four times to facilitate statistical analysis.

Ultrasound at 476 kHz, which we hereafter nominally call 500 kHz, was applied using a focused transducer (H-104B, Sonic Concepts, Woodinville, WA). A sinusoidal waveform was generated using a function generator (HP 33120A, Hewlett-Packard) and amplified with a RF power amplifier (240L ENI, Rochester, NY). The signal was sent to the transducer from the amplifier through a matching network (Sonic Concepts, Woodinville, WA) to minimize reflected power while being monitored with an oscilloscope. The experiments were carried out in an aluminum chamber (16 cm x 13 cm x 17.8 cm) filled with degassed water and containing acoustically absorbing rubber on the bottom and sides of the box in order to minimize reflections and standing waves.

Figure 4.1 shows the setup for 70 kHz; the chamber described above replaced the bath for the 500 kHz experiments.

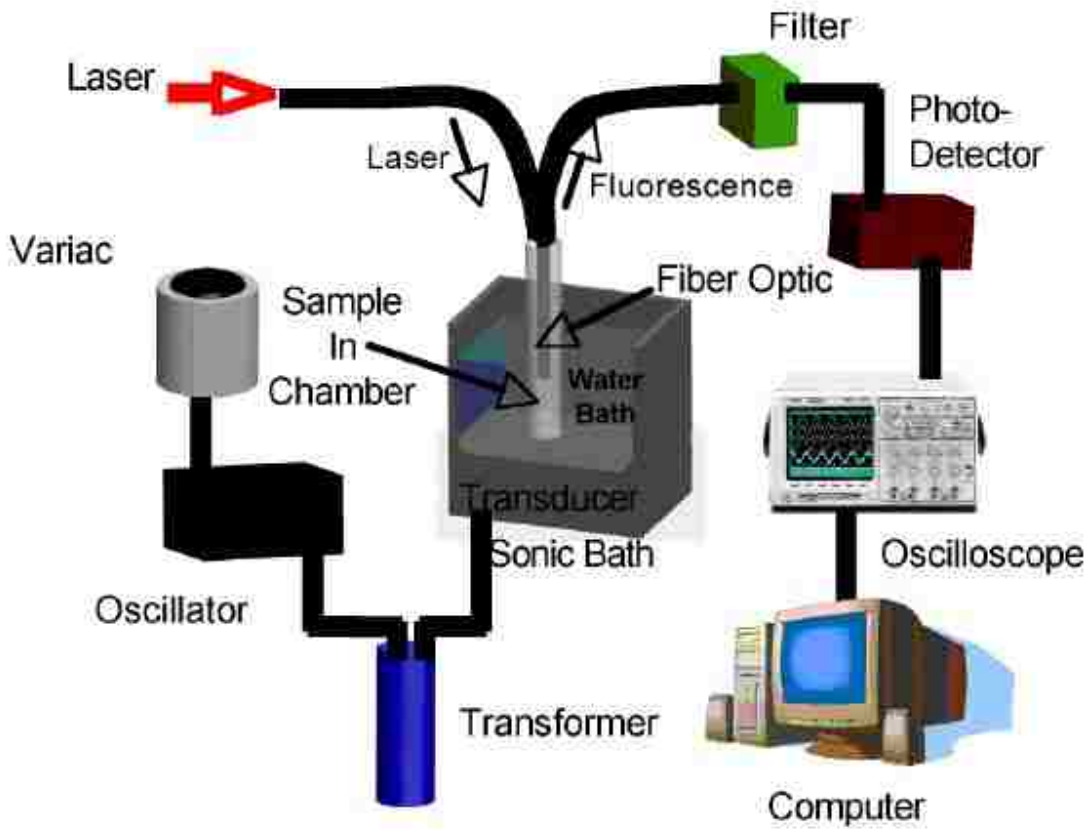


**Figure 4.1:** Experimental setup.

Since the US at 500 kHz is focused, the most acoustically intense spot (or focal point) is unique and so had to be carefully located before experiments began. The acoustic field of the transducer was mapped out by placing a calibrated needle hydrophone (HNR-1000, Onda, Sunnyvale, CA) within the transducer's field and systematically moving it across the three coordinate axes with the help of micrometers. These micrometers were attached to a base holding the hydrophone that also served as the top of the acoustic chamber. Once the focal point of the transducer was located, the Dox sample was placed there and the experiments proceeded as described above for 70 kHz. In this instance, however, the US intensities employed extended over a larger range than those used at 70 kHz, given that no previous data had been collected at these settings.

### 4.1.3 Monitoring of Acoustic Activity

To measure the ultrasonic power density delivered experimentally at 70 kHz, the output from the hydrophone (placed at the same intense spot as the sample) was recorded with an oscilloscope and then converted into an average acoustic intensity:

$$I_{AVE} = \frac{V_{RMS}^2 Q^2}{Z}, \tag{4.2}$$

where $V_{RMS}$ is the root-mean-squared voltage from the hydrophone, $Q$ is the manufacturer's frequency-dependent calibration factor, and $Z$ is the acoustic impedance of water ($1.5 \times 10^6$ kg/m$^2$/s). At 70 kHz, the conversion became

$$I_{AVE} = 0.1839 \ \frac{W}{cm^2 \ V_{RMS}^2} V_{RMS}^2$$

and, at 500 kHz,

$$I_{AVE} = 2.9785 \ \frac{W}{cm^2 \ V_{RMS}^2} V_{RMS}^2.$$

For the experiments at 500 kHz, the relationship between the voltage supplied ($V_{PP}^{in}$) and the voltage read by the hydrophone at the spot of highest intensity ($V_{RMS}^{hyd}$) was found to be (see Appendix A):

$$V_{RMS}^{hyd} = 10.368 \ V_{PP}^{in} + 0.0292 \ V,$$

and this voltage is the same voltage used in Equation (4.2) to calculate average acoustic intensity.

The acoustic chamber for 500 kHz described above also contained an orifice on a side wall through which the needle hydrophone was placed in order to monitor the acoustic activity within the chamber during the experiments.

The hydrophone signal for each run at 70 and 500 kHz was collected with an oscilloscope and the acoustic spectrum for each was obtained through the Fourier Transform of the signal.

### 4.1.4 Monitoring Radical Generation

A collapse cavitation event is strong enough to produce free radicals [64] whose rate of production can provide a quantifiable measure of collapse cavitation activity. The rate of OH radical formation under 500 kHz ultrasound was monitored by the reaction of hydroxyl radicals with iodide ($I^-$) ions in order to form iodine ($I_2$). A 70 mL solution of 0.03 wt% KI was sonicated for an hour with the same 500 kHz transducer described above at three different average intensities (374, 666, and 1040 W/cm$^2$) and circulated into a spectrophotometer (DU-640, Beckman Coulter, Fullerton, CA) which scanned the absorbance at 355 nm every fifteen seconds. This absorbance data was used to calculate a rate of iodine (and hence, hydroxyl radical) formation.

## 4.2 Mathematical Modeling

A MATLAB code that solves the Rayleigh-Plesset equation was written (Appendix B). The Rayleigh-Plesset equation is

$$\frac{p_V(T_\infty) - p_\infty(t)}{\rho_L} + \frac{p_{G_0}}{\rho_L}\left(\frac{R_0}{R}\right)^{3k} = R\ddot{R} + \frac{3}{2}\left(\dot{R}\right)^2 + \frac{4\nu_L\dot{R}}{R} + \frac{2S}{\rho_L R}, \qquad (4.3)$$

where $R$ is the bubble radius, $\rho_L$ and $\nu_L$ the density and kinematic viscosity of the liquid medium, respectively, $S$ is the surface tension at the bubble surface, $p_{G_0}$ is the partial pressure of the gas at some reference bubble radius $R_0$, $p_V$ is the vapor pressure at some temperature $T_\infty$ far from the bubble, $k$ is the polytropic constant, and the dot represents differentiation with respect to time. With the addition of a sinusoidal driving pressure $p_\infty(t) = p_{stat} + A\sin(2\pi ft)$, the Equation (4.3) is non-autonomous and highly non-linear and lacks an analytical solution except for limiting

cases [9]. For ease of computation, the equation was transformed into an autonomous, three-dimensional system of differential equations by introducing the variables $u = \dot{R}$ and $\Theta = ft \mod 1$. The system is then

$$\begin{aligned}
\dot{R} &= u \\
\dot{u} &= \frac{p_V(T_\infty) - p_{stat} - A\sin(2\pi\Theta)}{\rho_L R} + \left(\frac{p_{G_0}}{\rho_L R}\right)\left(\frac{R_0}{R}\right)^{3k} - \frac{3}{2}\frac{u^2}{R} \\
&\quad - 4\nu_L\frac{u}{R^2} - \frac{2S}{\rho_L R^2} \\
\dot{\Theta} &= f.
\end{aligned} \tag{4.4}$$

Hence, by moving the analysis into the state space $M = \mathbb{R}^+ \times \mathbb{R} \times S^1$, a simple MATLAB ODE solver (ode45) was used to numerically approximate the solution.

The first goal was to model the bubble behavior observed in the drug release experiments as closely as possible. In particular, frequency spectra corresponding to the acoustic spectra found experimentally were generated by computing the Fourier transform (MATLAB function fft) of the radial oscillations obtained as part of the numerical solution to the bubble equation.

Once the integration of the ODE system was in place, analysis was conducted on a qualitative level using several results from dynamical systems theory. Trajectories were plotted as functions of pressure amplitude and fixed frequency (70 and 500 kHz) and equilibrium bubble diameter (10 $\mu$m). Bifurcation values of the pressure amplitude parameter and the resulting routes to chaos were found and compared to the experimental values (both subharmonic and collapse cavitation thresholds).

Finally, the analysis was moved from the continuous to the discrete realm of dynamical systems by plotting Poincaré maps (maps of first return on a suitably defined hyperplane $\Sigma \subset M$, in this case a cut of $M$ transverse to the $\Theta$ direction yielding a projected plane on $u$ and $R$) of the system at parameters of interest (such as any thresholds and bifurcation locations). Orbit diagrams giving a more complete picture of the dynamic behavior of the system as pressure increased were created.

# Chapter 5

# *in vitro* Drug Release

The fluorescent properties of Dox were exploited as a probe for micellar drug release by tracking the dynamic quenching of its fluorescence upon sonication, which is a signal of release into the aqueous medium surrounding the micelle. In particular, *in vitro* drug release experiments at 70 kHz were conducted within 0 and 1 W/cm$^2$ while those at 500 kHz within 0 and 20 W/cm$^2$ in order to find any release thresholds indicative of cavitation-related phenomena. The role of cavitation was also explored by monitoring, by means of a hydrophone and spectrum analyzer, the acoustic spectra generated by the oscillating bubbles under the action of ultrasound, as explained in Chapter 4.

## 5.1 Drug Release at 500 kHz

No decrease in Dox fluorescence was detected at 500 kHz for intensities ranging from 0 to 20 W/cm$^2$. A typical fluorescence profile is shown in Fig. 5.1. The lack of change in fluorescence indicated that Dox molecules remained in the hydrophobic environment provided by the core of the P105 micelles when exposed to ultrasound. Hence, it is inferred that no Dox was released from P105 micelles at 500 kHz within the range of intensities indicated.

Acoustic spectra show the behavior of the bubbles by giving the intensity of oscillation readings as a function of frequency. For a group of bubbles driven at a given frequency $f$, it is expected that the strongest intensity reading will belong to $f$, called the fundamental frequency. This behavior is seen in Fig. 5.2, a representative spectrum at 500 kHz and for an applied average intensity of 1.53 W/cm$^2$. As the applied intensity increases, the peak grows stronger and the baseline shifts up (Fig. 5.3,

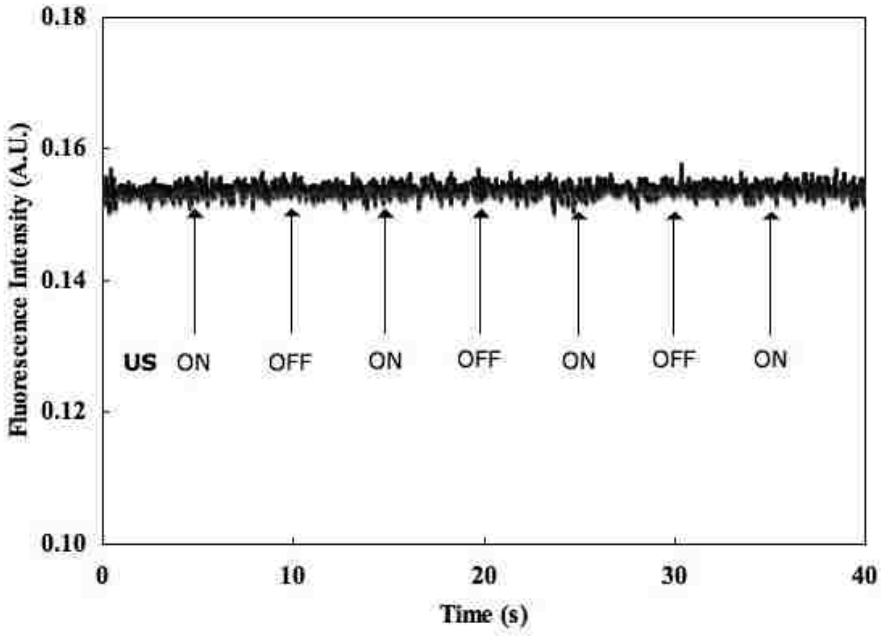


**Figure 5.1:** Fluorescence of P105-encapsulated Dox (in arbitrary units) during 500 kHz sonication. Average intensity during the pulse is 20 W/cm$^2$.

applied intensity of 195.8 W/cm$^2$). A shift in non-harmonic background emission is indicative of bubble collapse (a shock wave emitting all frequencies at the moment of collapse). Harmonic ($nf$, $n \in \mathbb{N}$) and a few ultraharmonic ($(2n+1)f/2$, $n \in \mathbb{N}$) peaks are present as well. The subharmonic peak, which is the signature most associated with both types of cavitation activity (see Section 2.2), never appeared at any of the intensities used.

According to the preceding results, no evidence of Dox release from P105 micelles using ultrasound at 500 kHz was found. Previous work by Husseini [27] has shown that drug release decreases with increasing frequency, and so high intensities are thought to be needed for release at 500 kHz. That intensities as high as 20 W/cm$^2$ failed to release Dox from micelles seems to disprove this prediction. The dependence may be nonlinear, however, which would mean that the necessary intensities may be outside the range used in this research. In that case, the applied pressures needed would exceed the accepted limits set for the safe medical use of ultrasound. These limits are defined by means of a parameter called the mechanical index (MI).

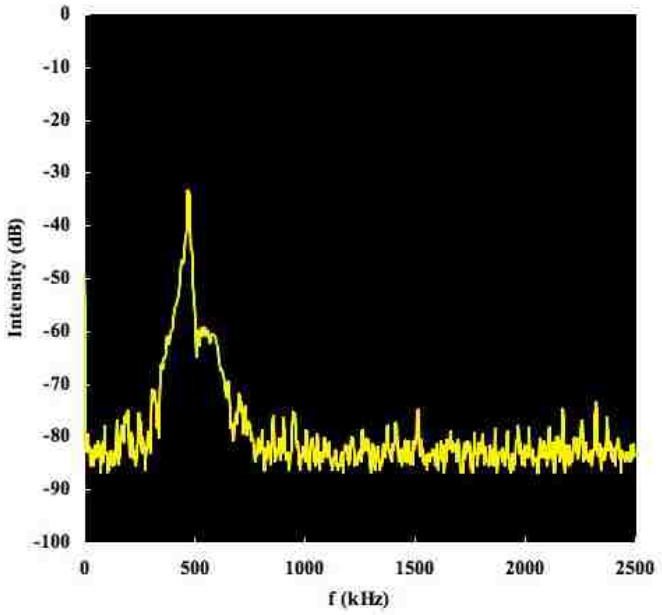


**Figure 5.2:** Acoustic spectrum for 500 kHz insonation, I = 1.53 W/cm$^2$.

Following the work of Apfel and Holland [3], the mechanical index was formulated by the American Institute of Ultrasound in Medicine as a measure of the likelihood of collapse cavitation occurring during ultrasound imaging [5]. It is defined as

$$MI = \frac{P^-/(1\ MPa)}{\sqrt{f/(1\ MHz)}},$$

where $P^-$ is the peak negative pressure and $f$ is the applied frequency in the units specified. Apfel and Holland reported that bioeffects and possible tissue damage can be expected for mechanical indices above 0.7 [3]. Barnett reported the more conservative value of 0.6 [5] and, elsewhere, cites an FDA upper limit of 0.23 for ophthalmologic exams [6]. In general, a value of MI above unity is considered unsafe and its use on humans is discouraged [6]. For these experiments at 500 kHz, the highest intensity used (20 W/cm$^2$) corresponds to a mechanical index of 10, clearly past the limits of safe use. This means that, if higher intensities than the ones used

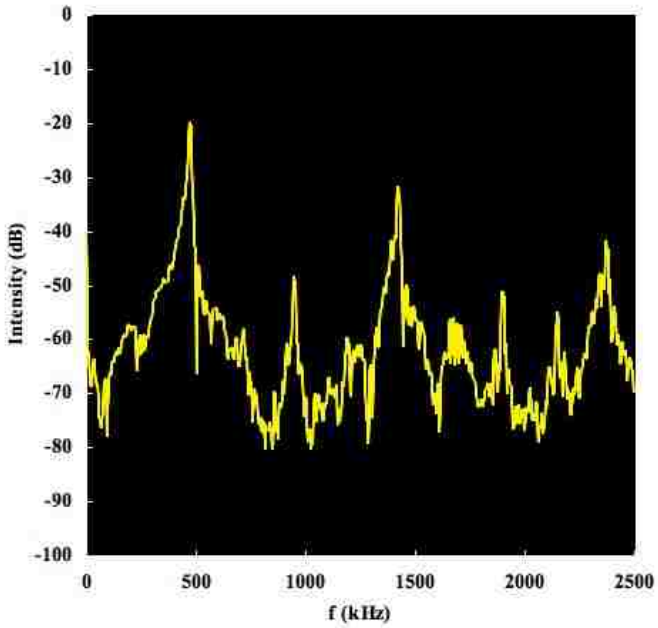


**Figure 5.3:** Acoustic spectrum for 500 kHz insonation, I = 195.8 W/cm$^2$.

in this research are indeed needed to release drug, they may not be of practical use in human therapy.

The high mechanical indices achieved in these experiments imply that inertial cavitation occurred but no drug was released. Hydroxyl radicals were generated at a rate of 0.78, 0.112, and 0.120 $\mu$moles/hour for applied intensities of 374, 666, and 1040 W/cm$^2$, respectively (see Section 4.1.4). Hence, as the applied intensity increased, radical generation (i.e., bubble collapse events) also increased. These intensities correspond to mechanical indices of 4.74, 6.32, and 7.90, well below the highest levels used in the drug release experiments. Radical monitoring and acoustic spectra suggested that, for sufficiently high intensities, bubble collapse occurs but the absence of a subharmonic signal raises doubts about the route followed by the bubbles to this eventual collapse. The clear harmonic oscillations that preceded the increase in broadband emission reflect the stable oscillations of the bubbles in the system up until the point of collapse. It appears that this type of bubble activity is unable to open P105 micelles and release their load. A comparison of this bubble behavior to

that which occurs under ultrasonic frequencies that are known to lead to drug release (70 kHz) should provide the answer.

## 5.2 Drug Release at 70 kHz

Release of doxorubicin from micelles using 70 kHz ultrasound has been reported [27], but while the data pointed to cavitation as the most likely mechanism, its role was not clearly explored. Deciphering the role of cavitation during drug release at 70 kHz and comparing it to bubble activity at 500 kHz is imperative if the absence of drug release at 500 kHz is to be explained. This information is found through the acoustic spectra generated by the bubbles and by the presence of any thresholds in drug release.

### 5.2.1 Pluronic™

Dox release from Pluronic™ micelles under 70 kHz US was tracked by the fluorescence detection system over a range of intensities between 0 and 0.8 W/cm$^2$. Measurements were repeated several times at each intensity level (n = 8 for I > 0.27 W/cm$^2$ and n = 4 for I $\leq$ W/cm$^2$) and averaged. Drug release from micelles was calculated as described in Section 4.1.1. The results are found in Fig. 5.4, which shows the percent of doxorubicin release (see Equation 4.1) as a function of the average power density delivered to the system.

The sigmoidal shape of the release profile reveals that percent release behaves nonlinearly with ultrasound intensity. Most tellingly, no significant (p > 0.05) change in fluorescence was detected below approximately 0.28 W/cm$^2$. At this intensity value there is a sudden onset of drug release which continues as intensity increases and eventually levels off. This is analogous to the bioeffect thresholds described previously. A similar threshold in bubble dynamic behavior at these power levels would associate drug release with cavitation activity, and so we turn to the acoustic spectra generated by the bubbles in the system.

Four representative acoustic spectra for these experiments using 70 kHz ultrasound are shown in Figure 5.5. Similarly to those seen in Section 5.1, they all show a

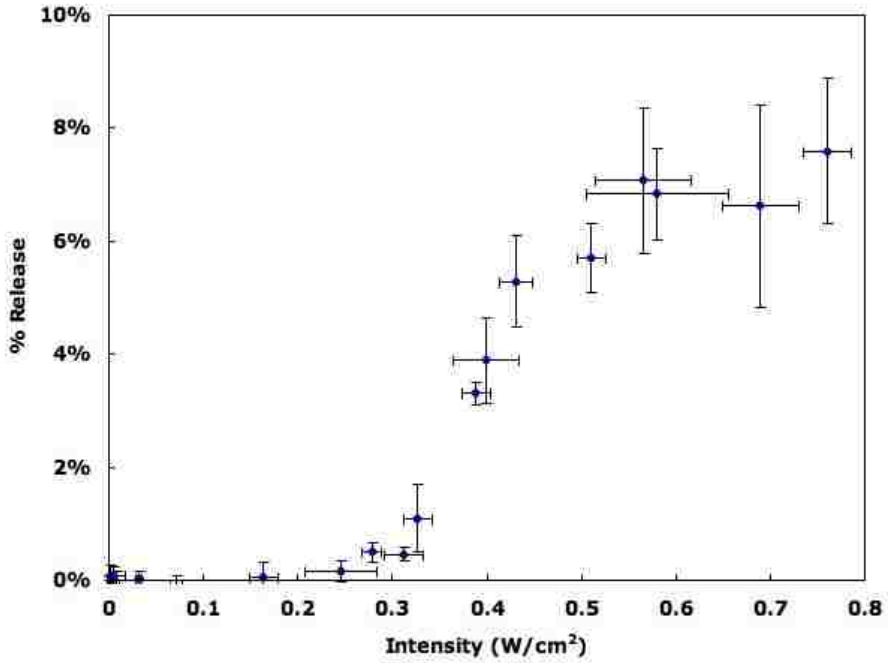


**Figure 5.4:** Average percent release of doxorubicin as a function of acoustic intensity at 70 kHz. Error bars represent standard deviations (n > 4) from the mean.

strong fundamental peak and several harmonics. The spectrum at I = 0.005 W/cm$^2$ (Fig. 5.5(a)) is analogous to Fig. 5.2, reflecting the stable oscillations of bubbles at the driving frequency and its integer multiples. However, they contain no subharmonic peak, the signal of interest.

The spectra shown in Fig. 5.5(b) and Fig. 5.5(c) for intensities of 0.25 and 0.28 W/cm$^2$, respectively, are significant as they present behavior that differs from that seen at 500 kHz. The former was taken at an intensity where no drug release was detected while the latter was taken at the onset of release (when the first measurable change in fluorescence was detected) and shows the development of a subharmonic peak at approximately 35 kHz. The baseline level also increases at this threshold, yet not for the first time, as Fig. 5.5(b) clearly shows a raised baseline. The spectrum at 0.52 W/cm$^2$ is shown as Fig. 5.5(d) for comparison and shows that as the applied intensity is increased, the magnitude of the subharmonic peak increases, as well as the level of the baseline.

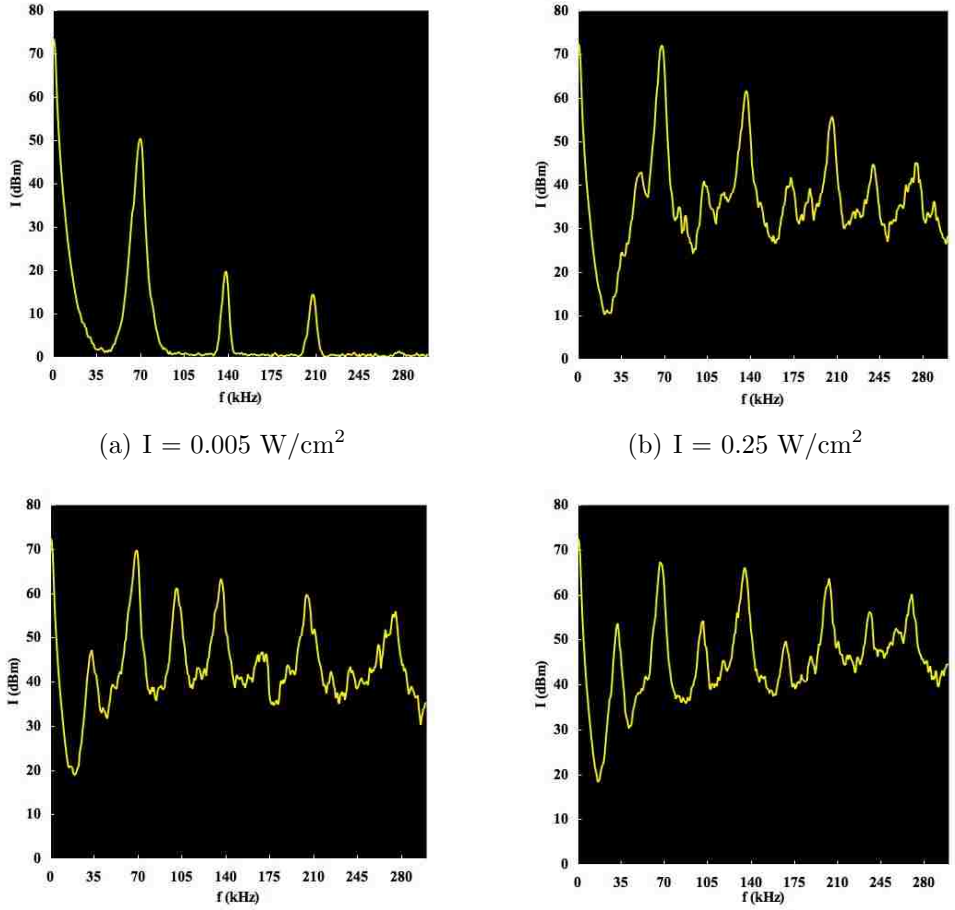


(a) I = 0.005 W/cm$^2$

(b) I = 0.25 W/cm$^2$

(c) I = 0.28 W/cm$^2$

(d) I = 0.52 W/cm$^2$

**Figure 5.5:** Acoustic spectra for 70 kHz insonation at I = (a) 0.005, (b) 0.25, (c) 0.28, and (d) 0.52 W/cm$^2$.

Thus, the onset of drug release corresponds to the emergence of the subharmonic signal in the acoustic spectrum. The spectra in Fig. 5.5 also suggest that the percentage of drug release increases as the magnitude of the subharmonic signal increases above baseline after the threshold. A correlation of this relationship is shown in Fig. 5.6, where the abscissa represents the logarithmic rise in subharmonic intensity above baseline and the ordinate represents the percent drug release from the micelles.

The preceding results merit careful analysis, as they hold a number of hints about the role that cavitation plays in ultrasonic drug delivery. In particular, there are two important phenomena which confirm the presence of cavitation activity in drug

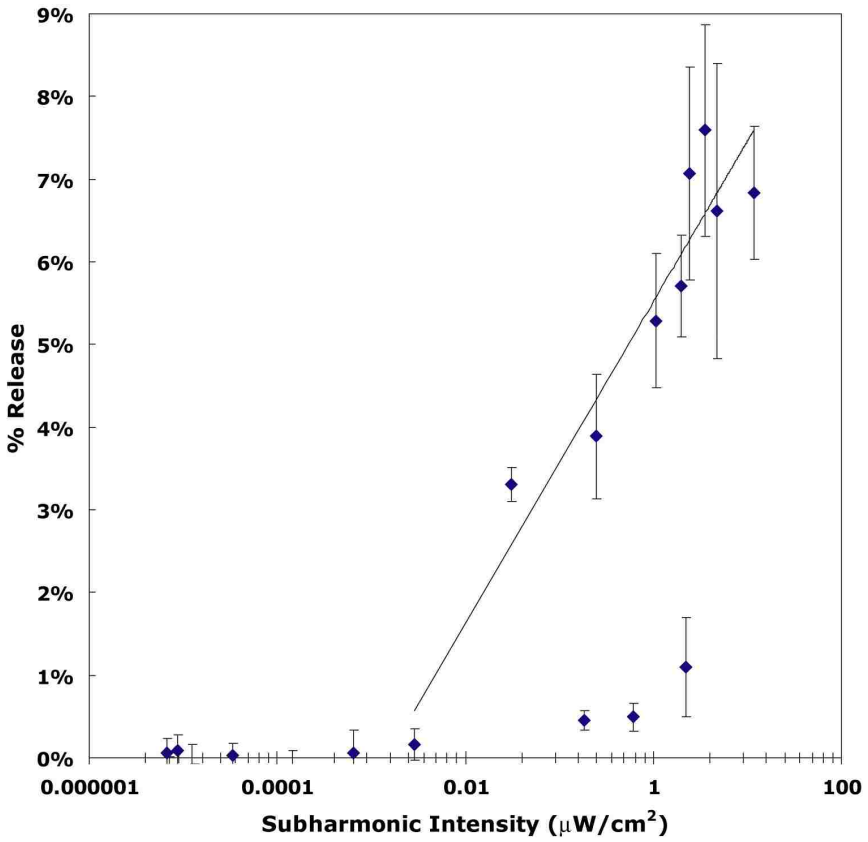


**Figure 5.6:** Percent doxorubicin release from Pluronic micelles correlated with the acoustic intensity of the subharmonic peak. Error bars represent standard deviations from the mean.

release: (1) the release and subharmonic thresholds and (2) the correlation between release and subharmonic intensity.

As explained in Section 2.2, thresholds for inertial cavitation are readily found in the literature and hence the behavior of the subharmonic signal in these experiments is not surprising. What is surprising is that it so clearly corresponds with the onset of drug release. Bio-effect thresholds are common as well [5, 21, 56, 64], varying with cell or tissue and type of effect sought, and they rarely coincide with the onset of collapse cavitation. Examples of bio-effect thresholds include 0.9 W/cm$^2$ for skin permeabilization at 76.6 kHz [90] and reach as high as 2000 W/cm$^2$ for DNA delivery to rabbit endothelial cells using 0.85 MHz ultrasound [25]. With such varied thresholds, the question naturally arises as to the type of cavitation associated with them

– specifically if inertial cavitation is needed for each. Cell membrane damage has been reported to occur in the region of stable cavitation [81], suggesting that bubble destruction (collapse) is not a necessary condition for many of these effects (though it is most likely sufficient due to the strong forces exhibited during the phenomenon). So it can be concluded that while the presence of both thresholds are definite signs of non-thermal ultrasound effects (cavitation), one cannot discard one or the other kind of cavitation based on this information alone. Furthermore, it still does not explain the absence of either a threshold for release or for subharmonic emission under 500 kHz ultrasound, given that, according to Tezel *et al.*, the bio-effect threshold should increase with increasing frequency [90] and not simply disappear.

Surely the origin of the subharmonic emission and its strong correlation with drug release holds the answer. Before delving into this, however, the three data points that are outliers to this correlation in Fig. 5.6 need an explanation. These points represent instances when the subharmonic signal noticeably appeared above the baseline with a relatively low percent drug release. All three also occurred in the applied intensity range of 0.27 to 0.34 W/cm$^2$, that is, right at the onsets of drug release and subharmonic emission. Near the latter, the subharmonic emission is said to be intermittent [48, 62] and chaotic [9]. Such intermittency may have caused the signal to be present long enough to be registered by the spectrum analyzer but not long enough to induce drug release (a time constant on the order of 200 ms [28]).

There exist a number of known studies associating a specific bio-effect with the subharmonic emission in the literature. These, just as the reports on the enduring debate about the origin of subharmonic signals, are nevertheless contradictory. Sundaram *et al.* reported that inertial cavitation was responsible for sonoporation of cell membranes since they were able to correlate 3T3 mouse cell viability and membrane permeability with acoustic white noise, which they also showed to be independent of subharmonic energy density [87]. On the other hand, Liu *et al.* were able to correlate hemolysis to subharmonic and ultraharmonic pressures but not broadband emission [49]. The root of these contradictions is found in the ongoing disagreement of whether the subharmonic signal is produced by stable or inertial cavitation.

Theoretical and experimental studies that associate the subharmonic emission with stable cavitation [2, 49, 51, 87] generally do so at intensities high enough to be considered close to the onset of collapse or under carefully controlled experimental conditions [51, 68] which generate stable nonlinear oscillations and are unlikely to be found in this experimental system. As mentioned in Chapter 2, the experiments of Phelps and Leighton [68] linking surface waves to subharmonic emission are illustrative of the debate in that they contradict Leighton's own previous conjecture [48] that a prolonged bubble expansion phase prior to collapse produces the signal. Others have reported correlations between the subharnonic signal and iodine release, sonoluminescence, and acoustic broadband emission [20, 21, 31, 62], all of which are evidences of bubble collapse.

The presence of signatures (other than the subharmonic) during drug release that are indisputably related to either type of cavitation may thus tilt the balance towards stable or collapse cavitation being behind micellar drug release. Such signals include, for example, radical generation and acoustic broadband emission, characteristic of bubble collapse [64]. Rapoport *et al.* captured free radicals with the spin trap 5,5-dimethyl-1-pyrroline-*N*-oxide (DMPO) using experimental conditions very close to the ones used in this research at intensities between 0.68 and 3.4 W/cm$^2$ [80]. While radicals were not trapped at the threshold intensity found in these experiments, the values are qualitatively close enough to presume that perhaps the amount of radicals generated at such low intensities was not large enough for measuring purposes. With regards to acoustic broadband emission, Figure 5.5 shows that the baseline does indeed shift at the onset of release (compare Fig. 5.5(b) and Fig. 5.5(c)), though, as noted before, not for the first time. That is, there is evidence that even before drug release, some bubbles were collapsing and generating acoustic signals containing the full frequency spectrum. Thus, one may conclude that at 70 kHz bubble collapse is present during the phenomenon that generates the subharmonic signal and correlates with drug release. These two signatures (radical trapping and broadband emission) are not correlated with release in the same way that the subharmonic signal is, how-

ever, and so care is imperative before declaring a definitive causal relationship between collapse cavitation and drug release.

As in Section 5.1, the Mechanical Index is also useful in the interpretation of these results. The MI for the drug release/subharmonic threshold shown in Figure 5.4 is 0.35, below the aforementioned tissue damage threshold. This MI value is interesting in that it is consistent with results by Shi *et al.* [85], wherein Sonazoid$^{TM}$ microbubbles were exposed to 2.5 MHz US and found to sustain nonviolent (i.e.: non-inertial cavitation) damage for intensities between 0.6 and 1.6 MPa, or between a MI of 0.4 and 1.0. For intensities above 1.6 MPa (MI $>$ 1.0), the bubble damage turned from a slow, gradual dissolution into a quick, disintegrating collapse. Hence, for values between MI of 0.4 and 1.0, bubble destruction is slow and gradual as opposed to a violent collapse. Shi *et al.* made no mention of the acoustic spectrum in their report, so it is difficult to know what kind of signature these damaged bubbles might generate. It is unlikely that they would generate the white noise associated with a violent collapse, which may mean that the baseline shift seen in Figure 5.5 may be due to peripehral bubbles which are closer to the resonance size and which may not necessarily be participating in the phenomenon responsible for drug release. It could then be argued that the subharmonic signal is really a measure of how much of this nonviolent damage is being inflicted on the bubbles present, which are eventually led to a slightly more stable collapse which is then able to release the drug load from the micelle.

Bubble interaction with different materials [51] and medium viscosity [23] influence the duration of stable cavitation and the threshold for collapse cavitation, respectively. These factors, together with the ultimate goal of medical application, suggested that investigation of the drug delivery system using stabilized micelles and different temperatures was necessary. This part of the research is covered in the next section.

### 5.2.2 Stabilized Micelles And Temperature Effect

If the drug delivery system studied in this research is ever to be used clinically, the micelle carrier must be stabilized in order to resist dissociation upon introduction into the bloodstream (see Section 2.1) and whatever cavitation phenomena responsible for release must be repeatable at physiologic temperature (37°C). To establish this, similar experiments were conducted using Pluronic$^{TM}$ at 37°C and 58°C as well as using the stabilized carriers Plurogel and PNHL at 37°C.

Analogous to the previous results, the percent release of Dox from the micelles is presented as a function of the applied power is shown in Figure 5.7. The data for all four experiments are included for comparison. The first and most obvious aspect of these results is that release from Pluronic$^{TM}$ is more than three times higher than from the stabilized carriers at the same temperature of 37°C.

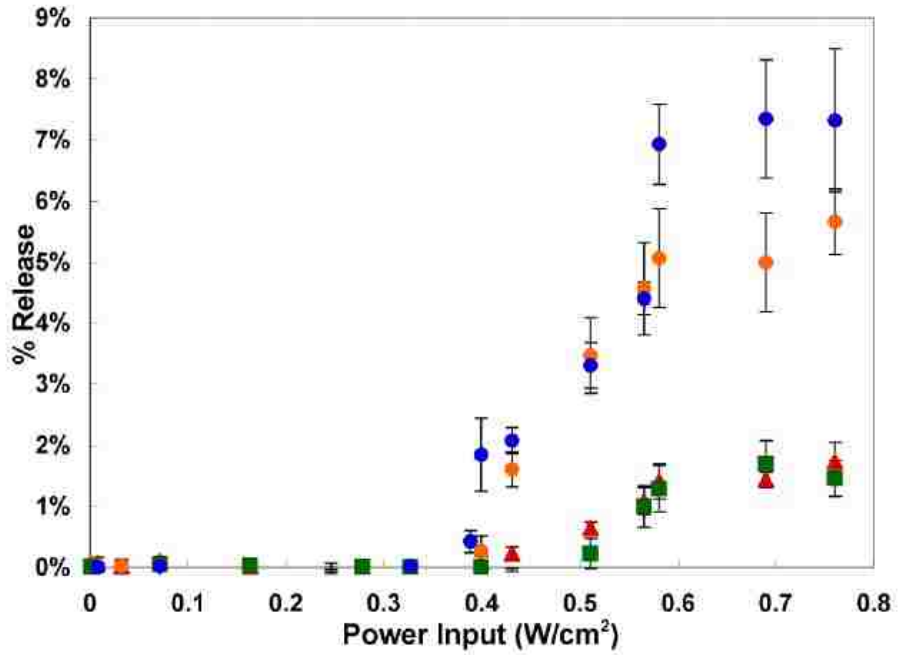


**Figure 5.7:** Average percent release of doxorubicin as a function of acoustic intensity at 70 kHz from unstabilized and stabilized micelles, ○: P105, 37°C; ○: P105, 58°C; □: Plurogel, 37°C; Δ: PNHL, 37°C. Error bars represent standard deviations (n > 4) from the mean.

Another immediately noticeable feature of Fig. 5.7 is that the release threshold seen before is here repeated and appears to be independent of carrier. While the percent release varies by carrier, the threshold intensity above which any significant decrease in fluorescence was recorded is the same for all: around 0.38 W/cm$^2$.

Just as before, representative acoustic spectra for these experiments are shown in Figure 5.8. The first spectrum (I = 0.43 W/cm$^2$) shows the behavior of the bubbles around the release threshold while the second shows it for higher intensities (I = 0.76 W/cm$^2$). No subharmonic signal was seen at lower intensities and there were no differences in bubble behavior as recorded by the Spectrum Analyzer among the different carriers or temperatures. The onset of the subharmonic corresponded with the threshold of drug release, just as it did in the previous experiments. Also, an increase in the background noise can be seen as the half-harmonic appears, together with an increase in the subharmonic intensity as the applied power is increased.

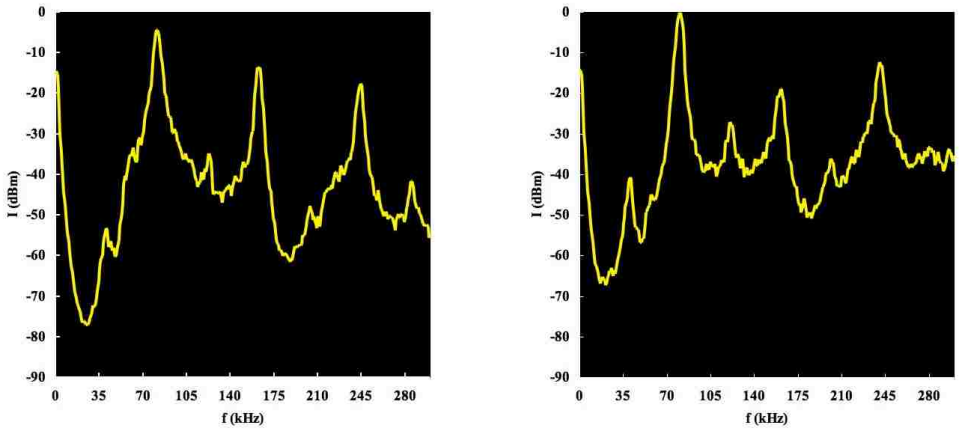


(a) I = 0.43 W/cm$^2$ (b) I = 0.76 W/cm$^2$

**Figure 5.8:** Acoustic spectra for 70 kHz insonation at I = (a) 0.43 and (b) 0.76 W/cm$^2$.

At this point, it is reasonable to anticipate that there might be a correlation between subharmonic intensity and drug release. These plots, similar to Figure 5.6, are shown in Figure 5.9 for Pluronic$^{TM}$ (Fig. 5.9(a)) and the stabilized compounds (Fig. 5.9(b)). There is an apparent linear relationship between the logarithmic in-

tensity of the subharmonic above noise level and drug release for Pluronic$^{TM}$ at both temperatures (confirming the previous result); yet, surprisingly, this fairly linear behavior is lost with the stabilized carriers.

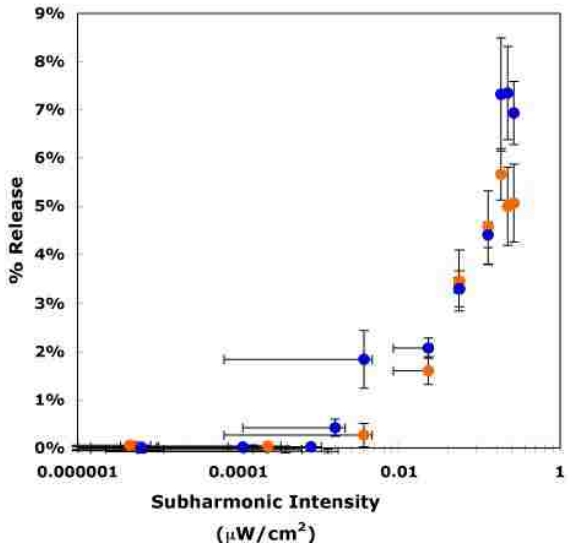


(a) P105 at 37 and 58$^o$C

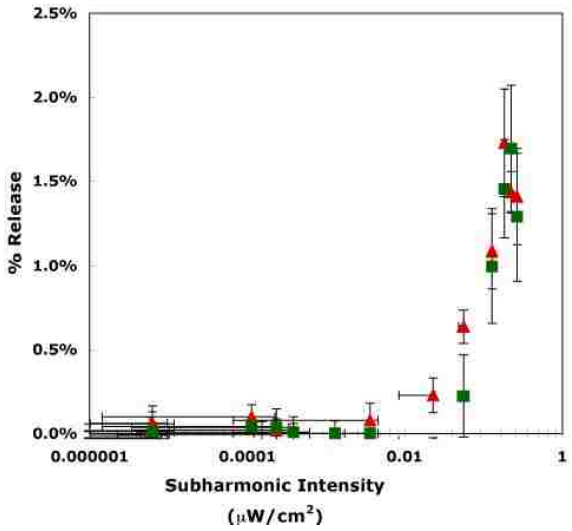


(b) Plurogel and PNHL at 37$^o$C

**Figure 5.9:** Percent Doxorubicin release as a function of subharmonic peak intensity of (a) ○: P105, 37°C; ○: P105, 58°C (non-stabilized micelles) and (b) □: Plurogel, 37°C; Δ: PNHL, 37°C (stabilized micelles). Error bars represent standard deviations from the mean.

Acoustic measurements reveal little more than they did in previous experiments. As before, the onset of release corresponds to the onset of the subharmonic signal for all compounds and at all temperatures. The same kind of baseline shift at the subharmonic threshold is also seen, one that is not necessarily a consequence of the subharmonic signal but more a function of the increase in applied pressure. Conversely, it is important to note that no subharmonic signal was ever seen in the absence of this increase in background noise. Nevertheless, one can say that, for all of these experiments, bubble collapse occurs before subharmonic oscillations are recorded and drug release is detected.

The mechanical index (MI) for the threshold in these experiments is 0.4, close to the value found for Pluronic$^{TM}$ at room temperature (0.35). This MI value is also the one reported by Shi *et al.* as the threshold for the "nonviolent destruction" of microbubbles discussed previously. Hence, we conclude that the same acoustic phenomenon (whatever it may be) is responsible for drug release from both stabilized and non-stabilized micelles and is independent of temperature.

Figure 5.7 suggests that percent drug release is a function of temperature and of the type of carrier. While drug release from Pluronic$^{TM}$ seems higher at 58°C than at 37°C, the difference between the slopes (0.25 and 0.24 % release/W/cm$^2$) of the two data sets is statistically insignificant ($p = 0.112$). The thresholds of release at 58°C and at 37°C were also estimated by linear extrapolation (0.355 and 0.379 W/cm$^2$, respectively), a difference which is marginally significant ($p = 0.035$). This effect can be understood by examining the effects of temperature on bubble dynamics. The effects of temperature are felt in the changing viscosity of the surrounding medium and in the vapor pressure of water within the bubble [9]; as temperature increases, water viscosity decreases, which in turn decreases the damping of bubble oscillations. Less damping of oscillations allows the bubble to reach a collapse event at lower acoustic intensities than would otherwise be needed [23]. Thus, an increase in medium temperature would have the overall effect of reducing the cavitation threshold, which is consistent with the results summarized in Fig. 5.7, where the threshold of drug release is reached at (barely significant) slightly lower intensities when the temperature

is increased. This temperature effect was not seen in the acoustic spectra collected, however, as both temperatures yielded basically the same acoustic readings. Two things explain this discrepancy: the temperature difference needed for such detection may be higher than the one employed (witness the p-value of 0.035) and the bubble dynamics system may be so chaotic and unstable that such resolution may be impossible with the equipment used. The chaotic behavior of the system studied is examined in more detail in the next chapter.

The unexpected result in these experiments is that the linear relationship between the logarithm of the subharmonic intensity and drug release is absent with stabilized micelles (Fig. 5.9). The linear correlation shown in Figure 5.9(a) is consistent with the results at room temperature shown in Figure 5.6 while the correlation for Plurogel in Figure 5.9(b) is nonlinear. A Plurogel micelle (see Section 2.1) is simply a P105 micelle with an interpenetrating network of *N*,*N*-diethyl acrylamide polymerized into its hydrophobic core. This nonlinear behavior and the fact that stabilized and cross-linked micelles release less than Pluronic$^{TM}$ micelles (Fig. 5.7) suggest that shearing is important to the release process. It appears that higher shear forces are necessary to induce release from these carriers since they have stronger stabilization forces when compared to micelles of P105.

It was mentioned previously that bubble collapse has been shown to not be necessary for certain bio-effects, but that collapse is normally assumed to be sufficient to produce bio-effects due to the shock waves and subsequent strong forces produced by the event. It is therefore disconcerting to find that although bubble collapse occurred at 500 kHz, no drug release was recorded, in an apparent contradiction to this claim. Bubble activity under 70 and 500 kHz applied ultrasound is explored theoretically in the next chapter, but it is pertinent at this point to consider the possibility that it may not significantly differ between the two frequencies. If that is the case, then the fluorescence detection system used in these (and previous) experiments must be critically reexamined. The system is, after all, only an indirect measure of drug release. The question of what phenomenon (other than drug release) could be causing changes in fluorescence would need to be addressed. The involvement of cavitation

and in particular of double-period oscillations should be tested in this regard, that is, could this type of bubble activity interfere with the light in the fluorescence detection system enough to create the illusion of fluorescence quenching of Dox? Of course, there is evidence found in this research which would seem to also contradict this line of logic. Decrease in fluorescence due to ultrasound is a signal that occurs with such repeatability that it seems unlikely to happen out of a number of bubbles simply interfering with the light in the same way every time. Also, and perhaps most importantly, the results presented here for stabilized and cross-linked micelles directly disprove this hypothesis. If decrease in fluorescence is indeed an artifact, one would expect to see the same amount of decrease regardless of the carrier being used, especially when the acoustic signatures generated are essentially the same as those found for Pluronic$^{TM}$. That we see significantly less fluorescence decrease for stabilized and cross-linked micelles reflects that the changes in the signal are related to changes in the Dox environment and not to some independent phenomenon. Nevertheless, future research should address improving (perhaps even completely revamping) the experimental system that monitors drug release. One such way would be to introduce (either coating the container or in the medium itself) a compound that selectively binds Dox and then to measure the change in Dox bound to this compound (a type of assay); this experiment would undoubtedly turn into a kinetic study of Dox binding due to Dox's equilibrium with its surrounding medium when encapsulated in a micelle.

# Chapter 6

# Ultrasound and Bubble Dynamics

Our investigation into the nature of ultrasonic drug release from polymeric micelles has so far revealed three important details: (1) cavitation is involved, (2) the subharmonic signal of the acoustic spectra generated by the bubbles in the medium correlates with drug release at a frequency of 70 kHz, and (3) this phenomenon is not present at 500 kHz. The first was suspected due to previous results [27], while the latter two were heretofore unknown; all results were obtained experimentally by means of the fluorescent detection system described in Section 4.1.1 and are summarized in Chapter 5. One is naturally left to inquire about the nature of the bubble oscillations that generate the subharmonic signal (and concomitant drug release) at 70 kHz and what is so exceptional about them that they are absent at 500 kHz. The field of bubble dynamics is concerned with these questions.

The history behind the mathematical modeling of bubble oscillations under an applied pressure field was briefly summarized in Section 2.3. Among those who have contributed to the understanding of this physical system, Lauterborn stands out in that he used the qualitative tools of chaos physics (dynamical systems) [46] to interpret the behavior of bubble oscillations [67], revealing a glimpse of the complex dynamics inherent within the governing equations. In this Chapter, we follow Lauterborn's lead by analyzing bubble oscillations at 70 and 500 kHz with similar tools. In particular, we seek to find the same (or analogous) experimental acoustic signatures through modeling and to explore bubble behavior in a neighborhood of the thresholds found in Chapter 5. If the dynamics at 70 and 500 kHz are vastly different we may find the answers to the two remaining questions: (1) what type of bubble behavior

is responsible for release and (2) precisely under what conditions can drug release be achieved.

### 6.1 Mathematical Model of Bubble Oscillator

In Section 4.2 the Noltingk-Neppiras-Poritsky modification of the classic Rayleigh-Plesset equation was introduced (4.3); it is presented here again:

$$\frac{p_V(T_\infty) - p_\infty(t)}{\rho_L} + \frac{p_{G_0}}{\rho_L}\left(\frac{R_0}{R}\right)^{3k} = R\ddot{R} + \frac{3}{2}\left(\dot{R}\right)^2 + \frac{4\nu_L\dot{R}}{R} + \frac{2S}{\rho_L R}. \tag{4.3}$$

This modification accounted for the bubble contents as a polytropic gas. The system was driven by a sinusoidal driving pressure:

$$p_\infty(t) = p_{stat} + A\sin(2\pi f t).$$

As explained in the same section, a MATLAB program (see Appendix B) was created that solved the following system of autonomous differential equations by means of the adaptive ODE solver ode45:

$$\begin{aligned}
\dot{R} &= u \\
\dot{u} &= \frac{p_V(T_\infty) - p_{stat} - A\sin(2\pi\Theta)}{\rho_L R} + \left(\frac{p_{G_0}}{\rho_L R}\right)\left(\frac{R_0}{R}\right)^{3k} - \frac{3}{2}\frac{u^2}{R} \\
&\quad - 4\nu_L\frac{u}{R^2} - \frac{2S}{\rho_L R^2} \\
\dot{\Theta} &= f.
\end{aligned} \tag{4.4}$$

Unfortunately, this formulation is incapable of yielding reliable information around the moment of collapse (when high temperatures and pressures are generated) since it fails to account for liquid compressibility [9]. Keller and Kolodner [36] and later Keller and Miksis [37] rectified this by introducing the Mach num-

ber into the equation. Their versions, however, require the driving pressure expression shown above to contain a retarding term in its argument (that is, $p_\infty(t) = p_{stat} + A\sin(2\pi f(t + R/c))$, where $c$ is the speed of sound in water) which complicates the definition of the Poincaré map later on. Parlitz *et al.* (under Lauterborn's auspices) ignore this term in their analysis and show that their modification and the Keller and Miksis equation are equivalent up to terms of order $\mathcal{O}(c^{-2})$, which terms are ignored during the derivation of the latter. Accordingly, we used the Parlitz modification of the Keller-Miksis model for the results presented in this chapter. The equation is

$$\left(1 - \frac{\dot{R}}{c}\right) R\ddot{R} + \frac{3}{2}\dot{R}^2\left(1 - \frac{\dot{R}}{3c}\right) = \left(1 - \frac{\dot{R}}{c}\right)\frac{P}{\rho_L} + \frac{R}{\rho_L c}\dot{P}, \tag{6.1}$$

where $P$ is given by

$$\begin{aligned} P = &\left(p_{stat} - p_V(T_\infty) + \frac{2S}{R_0}\right)\left(\frac{R_0}{R}\right)^{3k} - \frac{2S}{R} - \frac{4\mu_L\dot{R}}{R} \\ &- p_{stat} + p_V(T_\infty) - A\sin(2\pi f t), \end{aligned}$$

and all variables remain the same as before and $\mu_L$ is the dynamic viscosity.

We can now introduce the variables $u = \dot{R}$ and $\Theta = ft \mod 1$ just as before to transform the Keller-Miksis-Parlitz equation into a system of three autonomous differential equations:

$$\begin{aligned} \dot{R} &= u \\ \dot{u} &= \left[\left(1 - \frac{u}{c}\right)R + \frac{4\mu_L}{\rho_L c}\right]^{-1}\left[-\frac{u^2}{2}\left(3 - \frac{u}{c}\right) + \left(1 + (1-3k)\frac{u}{c}\right)\right. \\ &\quad \left(\frac{p_{stat} - p_V(T_\infty)}{\rho_L} + \frac{2S}{\rho_L R_0}\right)\left(\frac{R_0}{R}\right)^{3k} - \frac{2S}{\rho_L R} - \frac{4\mu_L}{\rho_L}\frac{u}{R} \\ &\quad \left. - \left(1 + \frac{u}{c}\right)\frac{p_{stat} - p_V(T_\infty) + A\sin(2\pi\Theta)}{\rho_L} - R\frac{2\pi f}{\rho_L c}A\cos(2\pi\Theta)\right] \\ \dot{\Theta} &= f. \end{aligned}$$

This system was solved, again, using a standard MATLAB adaptive solver (ode45, see Section B.2).

Difficulties in the integration of the system above arise when the bubble oscillations contain the sharp downward peaks which are characteristic of collapse. Either more sophisticated algorithms or a smaller time step can resolve this difficulty, adding to the computation time [67]. Parlitz *et al* circumvented this problem by integrating a topologically equivalent system that smoothed out the singularities. Their approach was used in this research whenever the integration procedure was unable to handle the singularities arising in the Keller-Miksis-Parlitz model and inevitably "blew up." Briefly, the original system was transformed into a new one that allowed for smoother oscillations but also retained all of its qualitative, topological properties. This is accomplished by means of a diffeomorphism. The following definitions are adapted from Devaney [14]:

**Definition 1.** Let $f : I \to \mathbb{R}$ be a function and $I \subseteq \mathbb{R}$. We say $f$ is of class $C^r$ on $I$ if $f^{(r)}$ exists and is continuous at all $x \in I$, where $f^{(r)}$ is the $r$-th derivative of $f$.

**Definition 2.** Let $f : I \to J$, $I, J \subseteq \mathbb{R}$, be a continuous bijection. The function $f$ is a homeomorphism if $f^{-1} : J \to I$ is also continuous.

**Definition 3.** Let $f : I \to J$, $I, J \subseteq \mathbb{R}$. The function $f$ is a $C^r$-diffeomorphism if $f$ is a $C^r$-homeomorphism such that $f^{-1}$ is also $C^r$.

Intuitively, a homeomorphism is a function that preserves all topological properties (that is, any property that can be defined by open sets) and homeomorphic spaces are thus topologically identical. A diffeomorphism is stronger in that this property is carried over to differentiability, which is appropriate in the case of our analysis of a vector field.

Parlitz *et al.* [67] define the following diffeomorphism from the state space $M = \mathbb{R}^+ \times \mathbb{R} \times S^1$ into its topologically equivalent space $M'$:

$$x_1 = \alpha \exp\left(\frac{\beta R}{R_0}\right), \quad x_2 = \gamma u \exp\left(\frac{\beta R}{R_0}\right), \quad x_3 = \Theta, \tag{6.2}$$

where the parameters $\alpha$, $\beta$, and $\gamma$ control the smoothness of the oscillations in the new space. Time is also rescaled:

$$t' = f_0 t,$$

where $f_0 = \alpha\beta/\gamma R_0$. The inverse map is, naturally,

$$R = \frac{R_0}{\beta} \ln\left(\frac{x_1}{\alpha}\right), \quad u = \frac{\alpha}{\gamma}\frac{x_2}{x_1}, \quad \Theta = x_3. \tag{6.3}$$

The new vector field is found by proper substitution:

$$\begin{aligned}
x_1' &= x_2 \\
x_2' &= x_1(y^2 + [(1 - p_9 y)\, z + p_{12}]^{-1} [(p_3 + p_4 y)\, y^2 + (p_5 - p_6 y)\, z^{-3k} \\
&\quad - (p_7 + p_8 y)\, z^{-1} - (1 + p_9 y)\, (p_{10} + p_2 \sin(2\pi x_3)) - p_{11} \cos(2\pi x_3)]) \\
x_3' &= p_1,
\end{aligned}$$

where, for notational convenience, we have introduced the new variables $y = \dfrac{x_2}{x_1}$ and $z = \dfrac{1}{\beta} \ln \dfrac{x_1}{\alpha}$ and defined $p_1 = \dfrac{f}{f_0}$, $p_2 = \dfrac{A}{\delta^2 \beta \rho_L}$, $p_3 = -\dfrac{3}{2\beta}$, $p_4 = \dfrac{\delta}{2\beta c}$, $p_5 = \dfrac{1}{\delta^2 \beta \rho_L}\left(p_{stat} - p_V(T_\infty) + \dfrac{2S}{R_0}\right)$, $p_6 = (1 - 3k)\, p_5 p_9$, $p_7 = \dfrac{2S}{\delta^2 \beta \rho_L R_0}$, $p_8 = \dfrac{4\mu_L}{\delta \beta \rho_L R_0}$, $p_9 = \dfrac{\delta}{c}$, $p_{10} = \dfrac{p_{stat} - p_V(T_\infty)}{\delta^2 \beta \rho_L}$, $p_{11} = \dfrac{2\pi f A R_0}{\delta^2 \beta \rho_L c}$, $p_{12} = \dfrac{4\mu_L}{\rho_L c R_0}$, and $\delta = \dfrac{\alpha}{\gamma}$. Differentiation is with respect to rescaled time. A new MATLAB program was written to solve this system whenever the inward oscillations leading to collapse calculated from Equation 6.1 became so pronounced that the standard solver (ode45) was unable to yield reasonable values. The values used for the control parameters in the transformation were: $\alpha = 1$, $\beta = 2$, and $\gamma = 0.001$, as reported by Parlitz *et al.* [67].

The initial conditions used were $R = 10$ $\mu$m, $u = 0$ m/s, and $\Theta = 0$. Trajectories were plotted once transients disappeared, which normally occurred after about 250 $\mu$s.

It is important to note that these models are, of course, an overly simplified reflection of the experimental conditions. First and foremost, the models trace the behavior of only a single bubble under an external applied pressure, ignoring the coupling effects found in bubble clusters [1, 50, 65]. We found this acceptable since we seek only a qualitative sketch of how a bubble behaves at the parameters at which the experiments were run. Second, the initial bubble size is kept constant for all frequencies and pressures used in these calculations. Again, the objective was to find the qualitative differences in bubble behavior between 70 and 500 kHz; one bubble size was reasonable. In effect, by doing so, we are looking at a slice of parameter space, a space which is vast and highly complex [67]. Also, even though Pluronic$^{TM}$ was present as a surfactant in the experiments its effect on bubble size distribution is negligible for purposes of comparison between the two frequencies (its effect on bubble dynamics is subject for future research). The bubble size used in these calculations was $R_0$ =10 $\mu$m, a standard size used in the literature when the medium is water at room temperature [46, 67]. Additionally, by considering a single bubble of a given initial size, it is easier to study an acoustic signal in particular. This helps to separate behavior directly related to drug release (such as the subharmonic) from acoustic signals that may not be directly related to it (such as baseline shift). This is exemplified in Figures 5.5 and 5.8, where only the subharmonic correlates with drug release and the background noise shift is most likely a result of collapsing bubbles of a different resonant size. Finally, there are two differences worth mentioning between the experiments at 70 and 500 kHz. While the signal used to drive the 500 kHz was a clean sine wave (and hence directly analogous to these numerical calculations), the signal generated by the 70 kHz bath is actually a 70 kHz wave amplitude modulated sinusoidally at about 0.12 kHz. This "noisiness" is enhanced by the actual geometry of the bath itself, thereby helping one of its primary purposes, which is the cleaning of laboratory equipment. This explains the noisy appearance of the 70 kHz spectra (Figs. 5.5 and 5.8) compared to the ones generated at 500 kHz (Figs. 5.2 and 5.3). The clean driving pressure used for calculations at 70 kHz is thus an approximation

deemed appropriate since we are interested solely in exploring the dynamics arising out of a frequency difference.

## 6.2 Bubble Behavior at 500 kHz

The bubble dynamics equations return the radial displacement and the bubble wall velocity as a function of time; representative time series are shown in Figure 6.1 for a driving pressure of 141.4 kPa, corresponding to a mechanical index (MI) of 0.20. These are equivalent to voltage measurements made by the hydrophone during experiments and were similarly Fourier transformed to obtain the frequency spectra of the bubble oscillations.

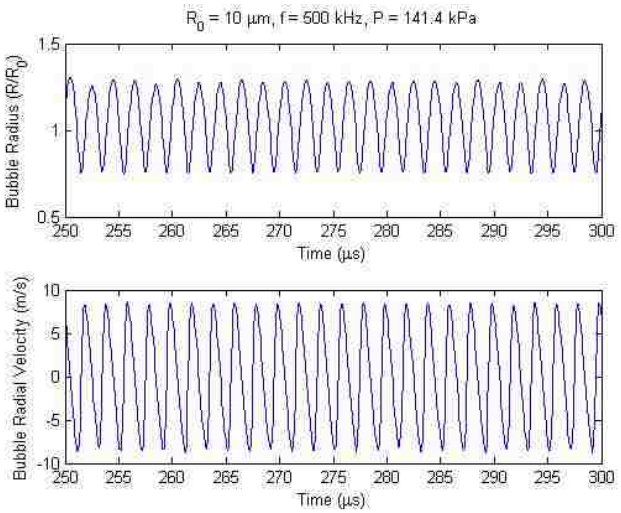


**Figure 6.1:** Radius-time and velocity-time curves for MI = 0.20.

The state space given by the equations described in the previous section is three-dimensional, so trajectories of any given initial conditions should trace a three-dimensional shape. The definition of the variable $\Theta$ leads to a convenient state space: the product of the conic section traced by the smooth oscillations ($\mathbb{R}^+ \times \mathbb{R}$) and $S^1$ gives a toruslike state space $M$. Hence, the evolution of the variable $\Theta$ reflects the number of revolutions of a particular trajectory around this state space. One can then generate a projection of both $R$ and $u$, eliminating $\Theta$ and investigating the resulting

phase portraits two-dimensionally. The result is a limit cycle (an isolated closed trajectory) that appears to (incorrectly) cross itself, a consequence of the elimination of the extra dimension.

We define the Poincaré map as follows (adapted from Strogatz [86]):

**Definition 4.** Consider an $n$-dimensional system $\dot{\mathbf{x}} = \mathbf{f}(\mathbf{x})$. Let $\Sigma$ be an $n-1$ dimensional surface of section, required to be transverse to the flow. The Poincaré map $P : \Sigma \to \Sigma$ is a mapping of $\Sigma$ to itself, obtained by following trajectories from one intersection with $\Sigma$ to the next. Let $\mathbf{x}_k \in \Sigma$ be the $k$th intersection, then the Poincaré map is defined by

$$\mathbf{x}_{k+1} = P(\mathbf{x}_k).$$

The Poincaré map is a powerful tool that allows one to move from the realm of continuous dynamical systems to the more intuitive world of discrete maps. Unfortunately, it is rarely possible to find an explicit form of the map. Here we rely on the numerical approximations of the ODE solver. Note that if $\mathbf{x}^*$ is a fixed point (i.e., $P(\mathbf{x}^*) = \mathbf{x}^*$), then a trajectory starting at $\mathbf{x}^*$ returns to $\mathbf{x}^*$ after some time $T$ and is therefore a closed orbit for the original system $\dot{\mathbf{x}} = \mathbf{f}(\mathbf{x})$. Hence, when plotting this map on $S$, any attracting limit cycles generated by the bubble equations will result in points on the plane. If the bubble is oscillating at the driving frequency $f$, a single point should appear. If the bubble, however, begins oscillations at twice the period of the applied pressure (that is to say, at half the frequency, $f/2$), then two points should appear on the plane, and so forth. In nonlinear dynamical systems such as the one analyzed here, it is common to find another type of attractor, called a strange attractor. This is no longer a point, curve, or surface, but a fractal, and will reveal itself on the Poincaré cross-section as a type of "smearing" of points with self-similar structure [46, 67, 86].

Bubble dynamics at 500 kHz follow a well-known dynamic pattern as the driving pressure increased. For low values of the applied pressure (in the case shown in Figure 6.2, A = 106.1 kPa, corresponding to a MI of 0.15), the oscillations settle

onto a stable limit cycle, a periodic orbit with period equal to that of the driving pressure (Fig. 6.2(a)). Accordingly, we see a single point in the Poincaré cross-section (Fig. 6.2(b)). This means, as expected, that the acoustic spectrum should have a single peak at the driving frequency (fundamental) $f = 500$ kHz (Fig. 6.2(c)).

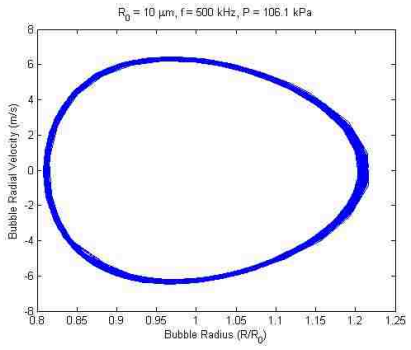


(a) Orbit, 500 kHz, MI = 0.15

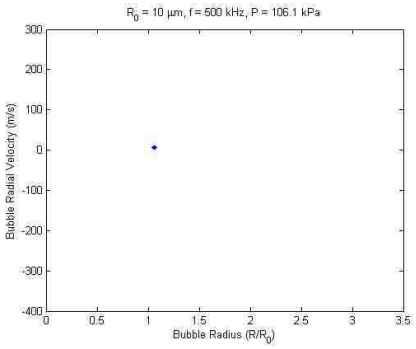


(b) Poincaré, 500 kHz, MI = 0.15

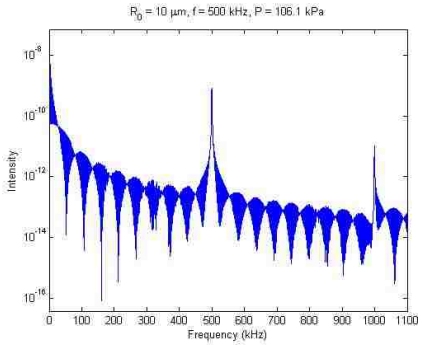


(c) FT, 500 kHz, MI = 0.15

**Figure 6.2:** For a single 10 $\mu$m bubble at 500 kHz applied pressure and at a MI = 0.15: (a) trajectory in state space projection, (b) Poincaré section plot, and (c) frequency spectrum.

These oscillations are considered stable since they attract nearby initial conditions and because, as can be seen in Figure 6.2(a), the velocity remains uniform enough that the orbit traces a simple ellipse (no significant acceleration is seen as the bubble expands or contracts). The thickness of the cycle is due the superposition of the curves traced by the orbit as it returns, which curves do not exactly agree due

to the numerical integration algorithm. Nevertheless, the cycle is stable, and this dynamic behavior persists until the bubble alters its period of oscillation.

At a pressure of about 195 kPa (MI $\approx$ 0.275), a second loop forms in the state space trajectory (Fig. 6.3(a)), as it appears the solution winds around once more before returning to the same point. This is clearly seen in the Poincaré plot for this case (Fig. 6.3(b)), where another point is born, signifying the doubling of the period of oscillation (it takes the solution two driving periods to come back to the same point in space). One then expects the frequency spectrum to develop a subharmonic peak (at $f/2 = 250$ kHz), which is seen in Figure 6.3(c). This is a classic example of a period-doubling bifurcation of cycles.

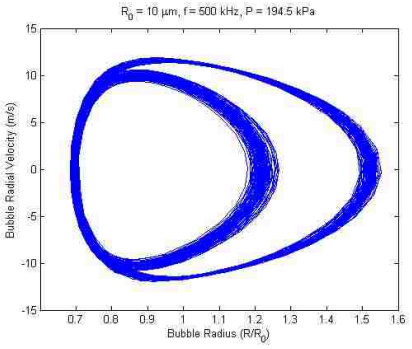


(a) Orbit, 500 kHz, MI = 0.275

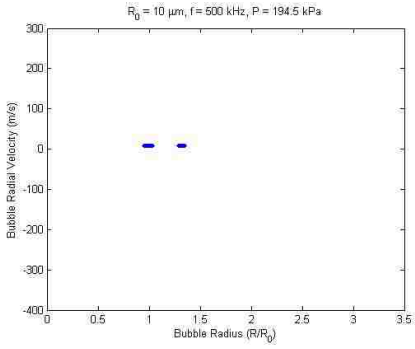


(b) Poincaré, 500 kHz, MI = 0.275

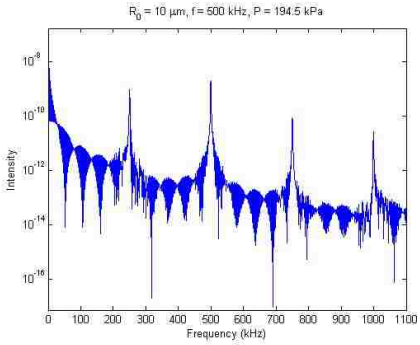


(c) Spectrum, 500 kHz, MI = 0.275

**Figure 6.3:** For a single 10 $\mu$m bubble at 500 kHz applied pressure and at a MI = 0.275: (a) trajectory in state space projection, (b) Poincaré section plot, and (c) frequency spectrum.

Figure 6.3(a) reveals more than just period doubling. It can be seen that the radial velocity begins to govern the dynamics of the bubble. While the maximum radius has only increased by about 25 %, the maximum velocity (which occurs at low radii) has doubled, hence the slightly lopsided appearance of the cycle. While this is all, of course, expected, it reveals the nonlinear nature of the oscillations, which becomes more evident as the accelerations at the moment immediately preceding and following collapse increase dramatically.

The appearance of the subharmonic peak at this MI value is puzzling as this was not seen experimentally (see Section 5.1). The biggest difference between the experiments and this model is, as mentioned above, the fact that only one bubble is modeled. This could mean that bubble clouds at the parameters above inhibit double-period oscillations. This remains to be explored. Another possibility is that the experimental setup was not accurate enough to reach this particular parameter value. This is unlikely since this double period persists for a range of close to 1 unit of MI, as explained below. On the other hand, the hydrophone may not have been able to clearly register the subharmonic signal. The matter is taken up again in the last section of this chapter.

As stated above, the dynamics remain the same (double-period cycles) until a pressure of about 233 kPa is reached (MI $\approx$ 0.33), at which point a new period-doubling bifurcation of cycles is encountered. The orbit diagram in Figure 6.4(a) does not explicitly show this new loop since it is so close to the original that it looks almost superimposed, but the Poincaré section plot (Fig. 6.4(b)) shows the creation of two more points on the plane. Most tellingly, the frequency spectrum shows peaks at $f/4 = 125$ kHz and its multiples (Fig. 6.4(c)).

The funnel-type shape of the limit cycle shown in Figure 6.4(a) contrasts with the one seen in Figure 6.3(a), which was rounder and smoother. The sharp acceleration at low radii reflects the bubble's increasingly violent behavior and augurs an impending collapse. A comparison of the spectrum in Figure 6.4(c) with Figure 6.3(c) reveals that, despite having undergone another period-doubling bifurcation, the baseline remains at the same level. This becomes important for subsequent pressure

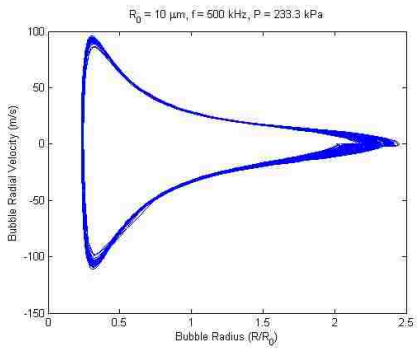


(a) Orbit, 500 kHz, MI = 0.33

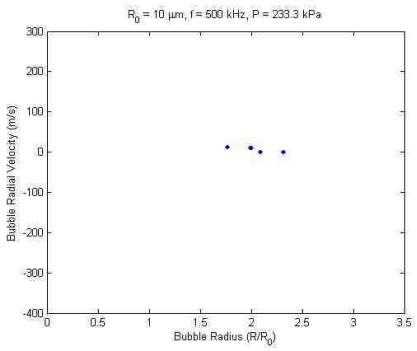


(b) Poincaré, 500 kHz, MI = 0.33

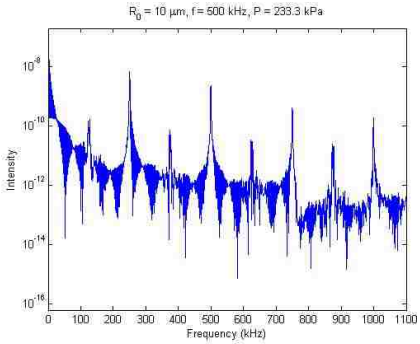


(c) Spectrum, 500 kHz, MI = 0.33

**Figure 6.4:** For a single 10 $\mu$m bubble at 500 kHz applied pressure and at a MI = 0.33: (a) trajectory in state space projection, (b) Poincaré section plot, and (c) frequency spectrum.

values and in the context of the relationship between the subharmonic signal and non-harmonic background shift.

Having seen two period-doublings, we would like to know if this behavior continues on indefinitely. This is precisely the case. The orbit shown in Figure 6.5(a) for an applied pressure of approximately 274 kPa (MI $\approx$ 0.875) reveals an increasingly complex trajectory which winds and twists "within" the projected orbit and stays preferentially at the highest velocities. Little can be gleamed from this orbit about the periods present at this pressure value but the frequency spectrum (Fig 6.5(c)) shows the clear emergence of a peak at $f/8 = 62.5$ kHz (and its multiples as ultraharmonics). The baseline has changed shape somewhat, becoming noisier and slightly leveling off the downward slope seen previously. This is most likely due to other frequencies that may be just outside the numerical accuracy in the spectrum but that start to appear

as a curve on the Poincaré cross-section (Fig. 6.5(b)), where no clear period 8 point can be seen.

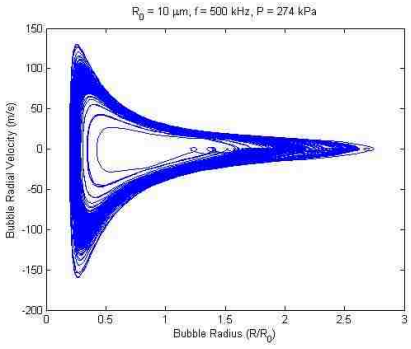


(a) Orbit, 500 kHz, MI = 0.3875

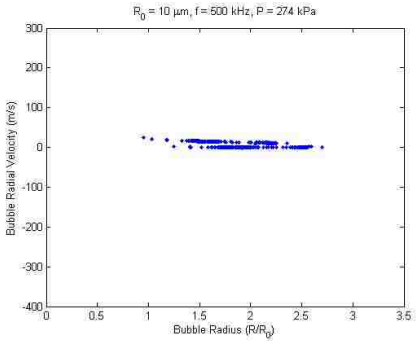


(b) Poincaré, 500 kHz, MI = 0.3875

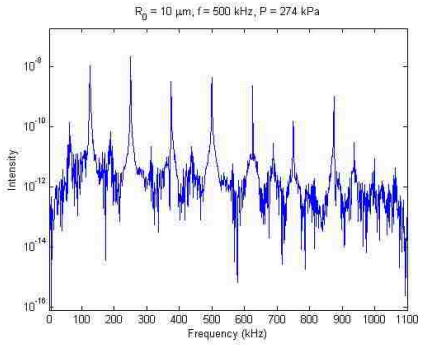


(c) Spectrum, 500 kHz, MI = 0.3875

**Figure 6.5:** For a single 10 $\mu$m bubble at 500 kHz applied pressure and at a MI = 0.3875: (a) trajectory in state space projection, (b) Poincaré section plot, and (c) frequency spectrum.

It is important to mention at this point that the MI values reported become more and more approximate as numerical resolution decreases and it becomes increasingly difficult to find bifurcation thresholds. That said, it is indisputable that another period-doubling bifurcation has occurred around the MI value reported above. This are the signs of what is known in dynamical systems theory as the *period-doubling route to chaos* [14]. We speak now, in particular, of the Poincaré map, which is a discrete map, since this "route to chaos" is defined for iterative maps of the line. We define a chaotic map properly in the last section of this chapter, but suffice it

to say that, roughly, we expect infinitely many periodic points in a chaotic regime (alternatively, all frequencies in the spectrum). This can only come from a strange attractor, speaking of continuous differential equations (such as the famous Lorenz equations). Indeed, a small perturbation in MI at the $f/8$ threshold shown above creates a strange attractor.

A small step in applied pressure from 274 (MI = 0.3875) to 274.4 kPa (MI = 0.388) reveals the strange attractor that provides the infinitely many periodic points characteristic of a chaotic map. Figure 6.6(a) shows the projection of this attractor, with its characteristic self-similar (fractal) structure, and is reminiscent of previous results in the literature that report on the chaotic attractors present in bubble dynamics [46, 67]. As expected, the Poincaré cross-section (Fig. 6.6(b) appears as more of a smear of points that retain, however, some sense of structure. Strangely, contrary to what is expected, the whole fractal image does not seem to be traced out on the plane; it seems the numerical solution is not seeing some frequencies. More revealing, then, is the frequency spectrum shown in Figure 6.6(c). The baseline does not seem altered in any significant way (which is expected from the Poincaré plot which fails to show all periods) but the appearance of third harmonics ($f/3$ and its multiples) stands out.

The peak at $f/3 = 166.6$ kHz in Figure 6.6(c) means that we have, in the discrete sense of the Poincaré map, a point of period three. Points of period three are important oddities in discrete dynamical systems, as expounded in the famous result of Sarkovskii. Consider the following ordering of $\mathbb{N}$ (known as Sarkovskii's ordering of the natural numbers):

$$3 \triangleright 5 \triangleright 7 \triangleright \cdots \triangleright 2 \cdot 3 \triangleright 2 \cdot 5 \triangleright \cdots \triangleright 2^2 \cdot 3 \triangleright 2^2 \cdot 5 \triangleright \cdots \triangleright 2^3 \cdot 3 \triangleright 2^3 \cdot 5 \triangleright \cdots \triangleright 2^3 \triangleright 2^2 \triangleright 2 \triangleright 1,$$

where all odd numbers (except 1) are listed first, followed by 2 times the odds, $2^2$ times the odds, and so forth, leaving the powers of 2 for last, followed by 1. The theorem is:

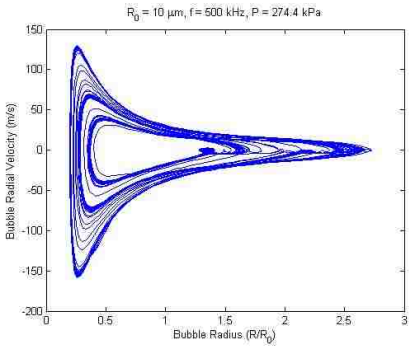


(a) Orbit, 500 kHz, MI = 0.388

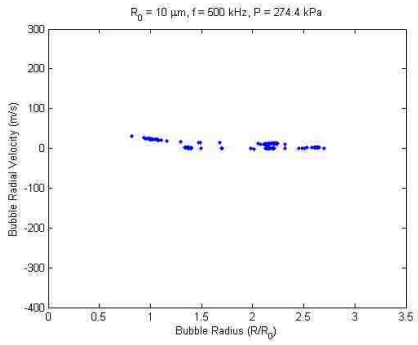


(b) Poincaré, 500 kHz, MI = 0.388

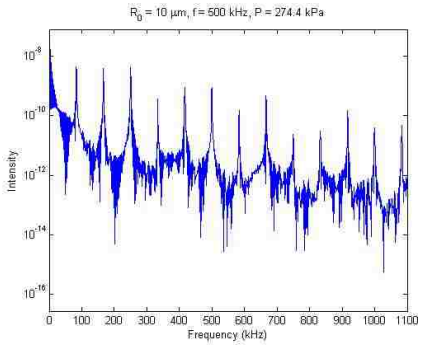


(c) Spectrum, 500 kHz, MI = 0.388

**Figure 6.6:** For a single 10 $\mu$m bubble at 500 kHz applied pressure and at a MI = 0.388: (a) trajectory in state space projection, (b) Poincaré section plot, and (c) frequency spectrum.

**Sarkovskii's Theorem.** Let $f : \mathbb{R} \to \mathbb{R}$ be continuous. Suppose $f$ has a periodic point of prime period $k$. If $k \triangleright l$ in the above ordering, then $f$ also has a periodic point of period $l$.

The theorem above is taken from Devaney [14], who also provides a basic proof. This theorem is remarkable for its simple hypothesis and strong result. The obvious corollary which concerns us is:

**Corollary.** Let $f : \mathbb{R} \to \mathbb{R}$ be continuous. Suppose $f$ has a periodic point of period three. Then $f$ has periodic points of all other periods.

Hence, by the Corollary above, if we restrict our Poincaré map to the real line (by, for example, collapsing it onto the radius or velocity axis) and it is continuous, then a periodic point of period three implies the existence of points of all other

periods. The theorem, however, says nothing about the stability of these points, and so while they may exist, they may not be stable and therefore invisible to the computer algorithm, which is most likely the case here. The stability of these points can be expected to change upon perturbation, however, thereby revealing them in the solution to the differential equations.

For pressures higher than 274.4 kPa (MI $>$ 0.388) the oscillations become chaotic and we finally see the periods that were absent in Figure 6.6. The representative results for A = 495 kPa (MI = 0.70) are shown in Figure 6.7. The beautiful self-similarity of the orbit is now even more clear (Fig. 6.7(a)), while the Poincaré cross-section (Fig. 6.7(b)) shows the fractal that we expected all along (notice that it shows a shape similar to the orbit). The frequency spectrum (Fig. 6.7(c)) now shows a noisy, raised baseline, a sign of the presence of all frequencies.

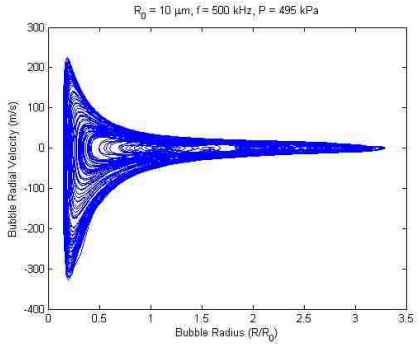


(a) Orbit, 500 kHz, MI = 0.70

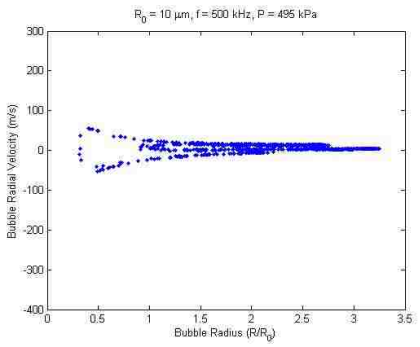


(b) Poincaré, 500 kHz, MI = 0.70

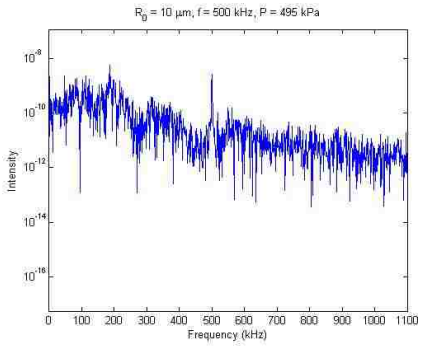


(c) Spectrum, 500 kHz, MI = 0.70

**Figure 6.7:** For a single 10 $\mu$m bubble at 500 kHz applied pressure and at a MI = 0.70: (a) trajectory in state space projection, (b) Poincaré section plot, and (c) frequency spectrum.

Thus we see that the dynamics of a 10 $\mu$m oscillating bubble with a driving frequency of 500 kHz follows the classic period-doubling route to chaos, starting at a MI of about 0.275. The oscillations reach chaos around MI = 0.388 and continue in the chaotic regime until at least a MI = 0.7. There are no stable regimes in this chaotic interval, except at MI $\approx$ 0.50 where a period three orbit is clearly seen again, implying (as previously seen) a brief change in the stability of the infinitely many periodic points that masks them from the numerical solution.

### 6.3 Bubble Behavior at 70 kHz

A bubble undergoes the period-doubling route to chaos at 500 kHz; we now question whether the same route to chaos is observed at 70 kHz (or if any chaos is reached at all). It turns out that the dynamics differ significantly at the lower frequency. Having introduced the majority of the qualitative tools previously, we immediately proceed to examine the dynamic behavior of bubbles at 70 kHz.

A stable limit cycle is created for low pressures just as in the 500 kHz case. The similarities end there, however, as Figure 6.8 reveals, which is a representative case with a pressure of 26.5 kPa (MI = 0.10). The orbit shown in Figure 6.8(a) is curiously different than its 500 kHz analog (Fig. 6.2(a)): it seems to be a mirror version with a slight pinching near $R_0$. The Poincaré cross-section (Fig. 6.8(b)) and frequency spectrum (Fig. 6.8(c)) show that the bubble is oscillating at the driving frequency and hence a single fixed point appears and the fundamental and second harmonic peaks are visible.

The "pinching" of the orbit reflects velocity variations as the bubble contracts and expands not seen at 500 kHz. In particular, the bubble achieves its highest velocities at its maximum radii, the exact opposite of what occurred at 500 kHz. Also, the bubble tends to momentarily slow down whenever it reaches a radius of about 99 % of its equilibrium radius $R_0$. Spectrum and Poincaré map-wise, however, the dynamics deceptively appear to be the same. Resonance may explain this phenomenon. For an air bubble in water at atmospheric pressure with an equilibrium radius $R_0$, the resonant frequency is reasonably approximated by [64]

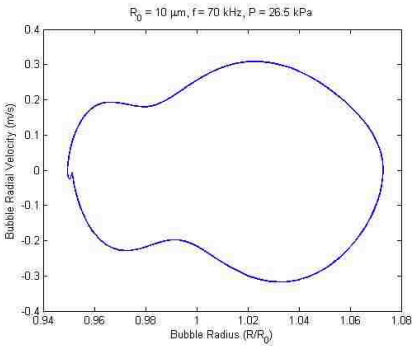


(a) Orbit, 70 kHz, MI = 0.10

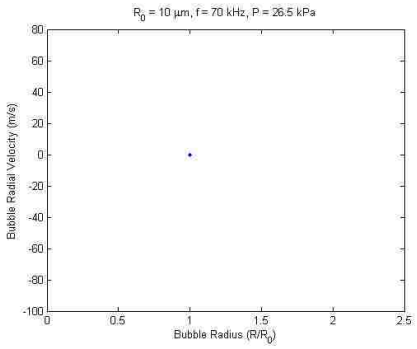


(b) Poincaré, 70 kHz, MI = 0.10

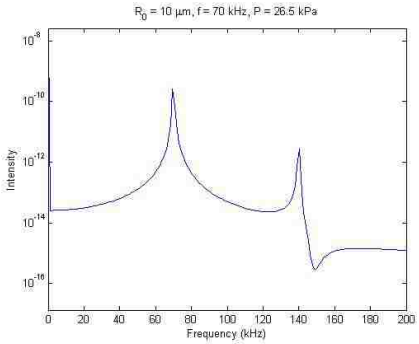


(c) Spectrum, 70 kHz, MI = 0.10

**Figure 6.8:** For a single 10 $\mu$m bubble at 70 kHz applied pressure and at a MI = 0.10: (a) trajectory in state space projection, (b) Poincaré section plot, and (c) frequency spectrum.

$$f_{res} = \frac{3.3 \text{ m/s}}{R_0}. \tag{6.4}$$

Hence, we can say that for a driving frequency of 70 kHz, the resonant bubble size is about 47 $\mu$m, while the resonant size at 500 kHz is 6.6 $\mu$m, much closer to the bubble size being modeled here. Hence, we can say that it is relatively "easier" for the bubble to oscillate at 500 kHz than at 70 kHz, explaining the bizarre behavior seen in Figure 6.8(a).

The solutions continue to show this "pinching" as the pressure is increased and the bubble oscillates at a frequency far removed from its resonance. Eventually, the acceleration of the bubble wall for low radii takes over and we see an orbit that

seems slightly more familiar, where the highest velocities are achieved at low radii, as seen in Figure 6.9(a). The pressure in Figure 6.9 is 84.7 kPa with a MI = 0.32. The orbit looks like a complicated series of twists and turns, yet the Poincaré cross-section (Fig. 6.9(b)) reveals a surprising detail: the period has doubled, showing two clear isolated points. The frequency spectrum (Fig. 6.9(c)) confirms this, showing the appearance of the subharmonic ($f/2 = 35$ kHz) signal.

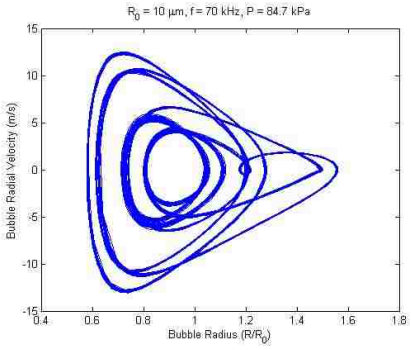


(a) Orbit, 70 kHz, MI = 0.32

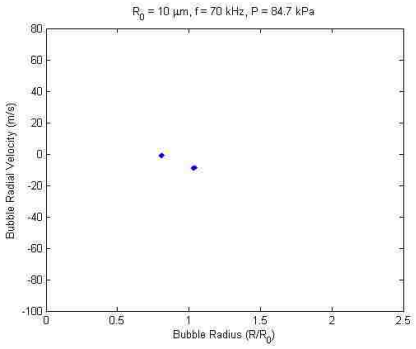


(b) Poincaré, 70 kHz, MI = 0.32

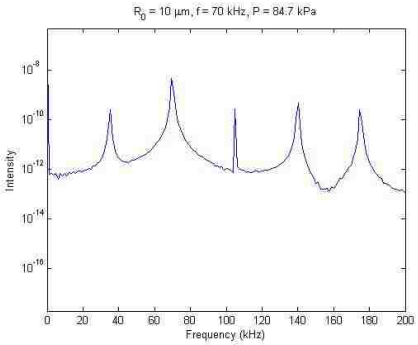


(c) Spectrum, 70 kHz, MI = 0.32

**Figure 6.9:** For a single 10 $\mu$m bubble at 70 kHz applied pressure and at a MI = 0.32: (a) trajectory in state space projection, (b) Poincaré section plot, and (c) frequency spectrum.

The orbit seen when the 500 kHz system underwent period-doubling (Fig. 6.3(a) contrasts with the present case. The former shows a clean doubling of the original cycle while the latter winds around numerous times before finally returning to itself. The "velocity pinching" mentioned before remains as well. In fact, it seems that, as

the pressure increases, the bubble struggles with being out of phase with the incoming wave more and more, leading to a jagged velocity profile.

The period doubles at MI = 0.32, the theoretical subharmonic threshold. Note that, from the results found in Chapter 5, the experimental threshold (in MI) was found to occur between 0.35 and 0.40. Considering the limitations of the model presented here (see Section 6.1), especially the fact that a single bubble is being studied and not a more realistic cluster of bubbles, the values show remarkable agreement. This suggests that, at least as far as subharmonics go, bubble interaction does not change the dynamics significantly. Or rather, that bubble interaction is not the dominant parameter at these conditions.

This double-period orbit continues for a number of pressures until the trajectories slowly move towards each other before seemingly coalescing into one. At a pressure of about 90.9 kPa, (MI $\approx$ 0.3435), we see that the solution trajectory has settled into a rather less complicated set than before (Fig. 6.10(a)). The Poincaré map (Fig. 6.10(b)) shows the two points almost superimposed on one another, effectively becoming a fixed point again. Half-frequency signals are barely visible in Figure 6.10(c), suggesting that the second period survives but is close to disappearing.

This is a drastic departure from what was seen at 500 kHz. At the higher frequency, after the first period doubling, the two points on the Poincaré cross-section slowly moved apart until they bifurcated in a second period-doubling. At 70 kHz, the second period solution appears to exist only momentarily before collapsing back into a single fundamental mode. A second period-doubling is absent and instead we find sudden chaos, as explained in the next paragraph.

Slightly perturbing the driving pressure after the seeming disappearance of the double-period orbit unexpectedly sends the system into chaos. Figure 6.11 presents results for a pressure of 92.6 kPa (MI = 0.35) almost immediately proceeding the stable double-period orbit shown above. The orbit projection (Fig. 6.11(a)) reveals the strange attractor that is created, which looks similar to the one found at 500 kHz (Fig. 6.7(a)), except for the large accelerations in the latter (which is at a high MI). Although the Poincaré cross-section (Fig. 6.11(b)) does not yet show a complete

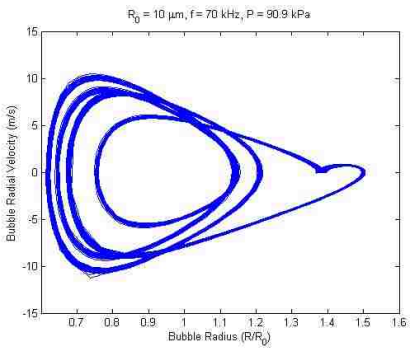


(a) Orbit, 70 kHz, MI = 0.3435

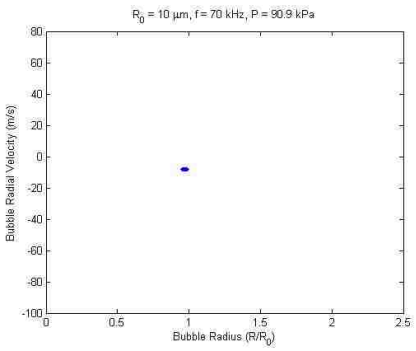


(b) Poincaré, 70 kHz, MI = 0.3435

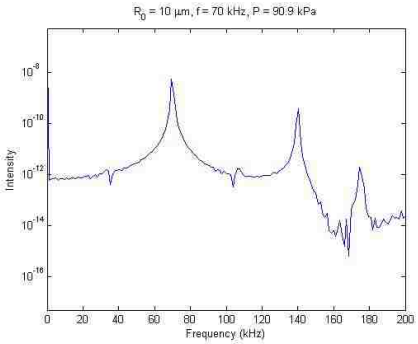


(c) Spectrum, 70 kHz, MI = 0.3435

**Figure 6.10:** For a single 10 $\mu$m bubble at 70 kHz applied pressure and at a MI = 0.3435: (a) trajectory in state space projection, (b) Poincaré section plot, and (c) frequency spectrum.

fractal shape, the frequency spectrum confirms the chaos created with its noisy, raised baseline (Fig. 6.11(c)).

The results of figure 6.11 find the bubble eschewing the route to chaos by a series of infinitely many period doublings seen in the previous section. Instead, the bubble oscillation develops a double period for a short time before creating all periods almost instantly. This apparently direct and sudden transition from some type of stable oscillation into a strange attractor is generally known as the *intermittent route to chaos* [69]. It arises out of a kind of bifurcation known as a saddle-node bifurcation of cycles (or fold), which, roughly, is concerned with the birth and/or destruction of stable and unstable limit cycles [22, 86]. All it takes to reach chaos is a single saddle-node bifurcation, although it could be the result of a series of them; the presence of this type of route to chaos in bubble oscillators has been reported by Lauterborn [46].

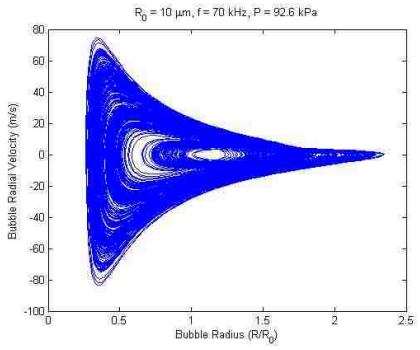


(a) Orbit, 70 kHz, MI = 0.35

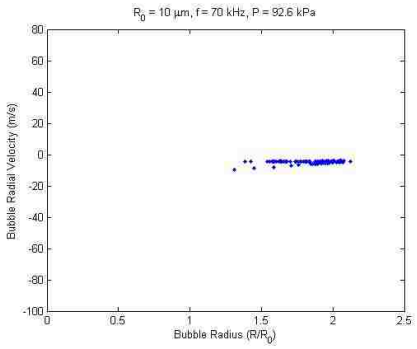


(b) Poincaré, 70 kHz, MI = 0.35

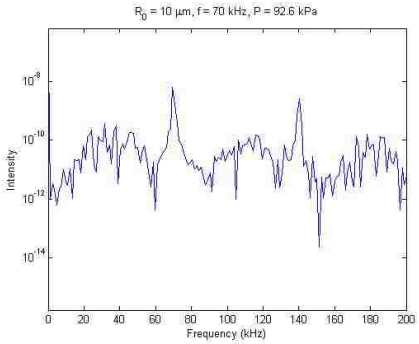


(c) Spectrum, 70 kHz, MI = 0.35

**Figure 6.11:** For a single 10 $\mu$m bubble at 70 kHz applied pressure and at a MI = 0.35: (a) trajectory in state space projection, (b) Poincaré section plot, and (c) frequency spectrum.

The resulting chaotic oscillations persist before ending as abruptly as they commenced, unlike the case at 500 kHz where, once chaos is reached, it remains indefinitely (up to MI = 0.70). At approximately 114 kPa (MI $\approx$ 0.43), a stable limit cycle is created out of the strange attractor (Fig. 6.12(a)). The Poincaré cross-section (Fig. 6.12(b)) accordingly shows a fixed point while the return of the fundamental peak (and its integer harmonics) is seen in the frequency spectrum (Fig. 6.12(c)).

It is noteworthy not only that the strange attractor disappears and a single-period stable limit cycle is created but that this new oscillation is not necessarily a return to the original fundamental oscillation (for MI $<$ 0.32). A comparison of Figures 6.8(a) and 6.12(a) shows that the new cycle is not only wider but also quite faster, with dramatic accelerations at low radii. The maximum inward velocity in Fig. 6.12(a) is revealing in that it has exceeded the speed of sound in air at the

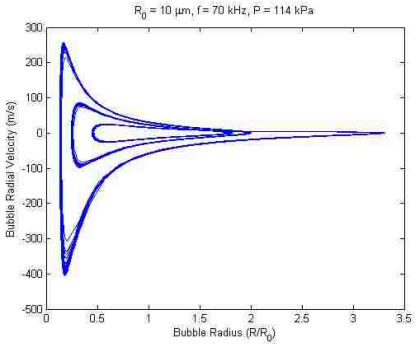


(a) Orbit, 70 kHz, MI = 0.43

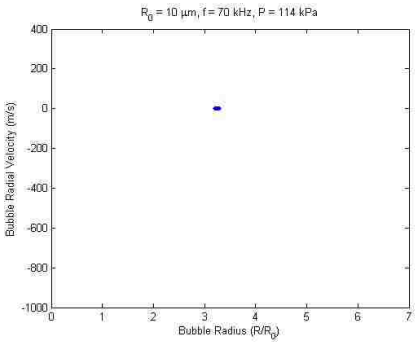


(b) Poincaré, 70 kHz, MI = 0.43

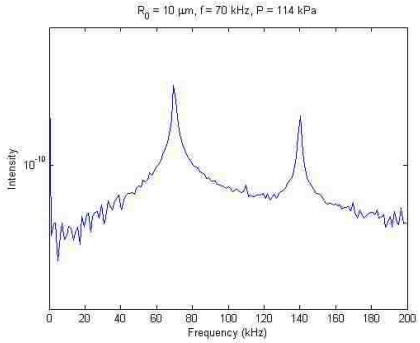


(c) Spectrum, 70 kHz, MI = 0.43

**Figure 6.12:** For a single 10 $\mu$m bubble at 70 kHz applied pressure and at a MI = 0.43: (a) trajectory in state space projection, (b) Poincaré section plot, and (c) frequency spectrum.

simulation conditions, which is approximately 350 m/s. This is most likely evidence of a bubble collapse as the incoming bubble wall is moving faster than the speed of sound of the vapor, creating a density discontinuity and a shock wave. The model predicts a symmetric collapse and so mathematically the bubble "bounces back" to continue oscillating. In reality, the bubble will collapse asymmetrically and fragment into smaller bubbles. As will be shown shortly, for increasing pressures, the bubble wall velocity will continue to exhibit this behavior, and we can say that the bubble is in a collapsing regime. The oscillations, however, do not remain as a stable limit cycle and so we investigate how the new chaotic regime is achieved.

First, at some point just before A = 132 kPa (MI = 0.50), the system undergoes another period-doubling bifurcation (Fig. 6.13). A close examination of the resulting limit cycle in Figure 6.13(a) reveals the second loop trailing closely to the

original cycle, leading to a second point on the Poincaré plot (Fig. 6.13(b)) and the reemergence of the subharmonic peak in the frequency spectrum (Fig. 6.13(c)).

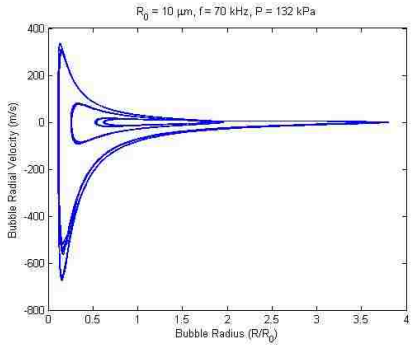


(a) Orbit, 70 kHz, MI = 0.50

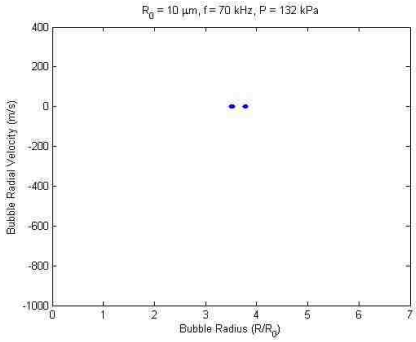


(b) Poincaré, 70 kHz, MI = 0.50

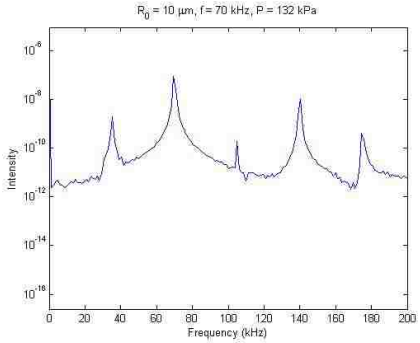


(c) Spectrum, 70 kHz, MI = 0.50

**Figure 6.13:** For a single 10 $\mu$m bubble at 70 kHz applied pressure and at a MI = 0.50: (a) trajectory in state space projection, (b) Poincaré section plot, and (c) frequency spectrum.

The bubble's motions keep increasing in velocity as it collapses, as the projected orbit shows in Figure 6.13(a). The velocity is close to zero at the equilibrium radius with most of the acceleration concentrated at very low radii, close to collapse. Also, the bubble wall achieves its maximum velocity as it contracts close to collapse, almost twice the velocity attained as it expands.

The bubble's behavior is starting to look familiar. Instead of creating a single-period oscillation before launching into chaos however, the two points on the Poincaré plot keep moving apart from each other. At a pressure of about 140 kPa (MI $\approx$ 0.53),

the first indications of chaos begin to appear (Fig. 6.14). The strange attractor is not clearly visible yet (the cycle seems to be slowly winding into itself, see Figure 6.14(a)), the system appears to be stuck in the transition between stable double-period oscillations and chaos, as seen in the frequency spectrum (Fig. 6.14(c)), where the subharmonic remains amidst a raised and noisy baseline. This behavior is common in the intermittent route to chaos, where the system moves between stable oscillations (at the period immediately preceding chaos) and short bursts of chaotic motion (hence, "intermittent"). These "laminar phases" eventually disappear into full chaos [46]. Predictably, the Poincaré cross-section (Fig. 6.14(b)) begins to show the stretching of periodic points as they start to form the fractal indicative of chaos.

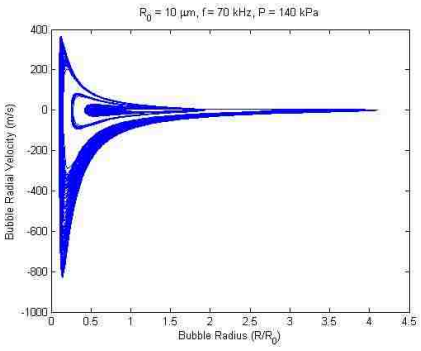


(a) Orbit, 70 kHz, MI = 0.53

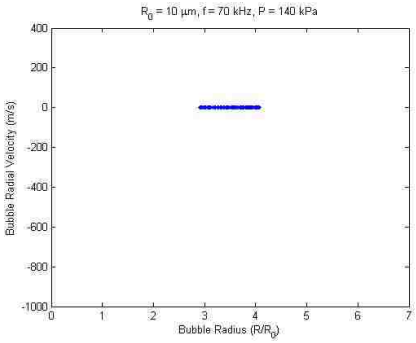


(b) Poincaré, 70 kHz, MI = 0.53

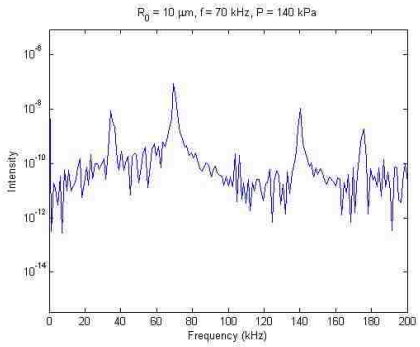


(c) Spectrum, 70 kHz, MI = 0.53

**Figure 6.14:** For a single 10 $\mu$m bubble at 70 kHz applied pressure and at a MI = 0.53: (a) trajectory in state space projection, (b) Poincaré section plot, and (c) frequency spectrum.

A new strange attractor is formed for values of A > 140 (MI > 0.53) containing oscillations of all periods. This is verified in a way similar to what was done at 500 kHz. There are several windows within the chaotic regime where oscillations of period three are present, such as at A = 148 kPa (MI = 0.56) (Fig. 6.15). The orbit (Fig. 6.15(a)) looks self-similar but without a multitude of winding trajectories within it resulting from all periods being present (hinting that they may be temporarily invisible to the computer).

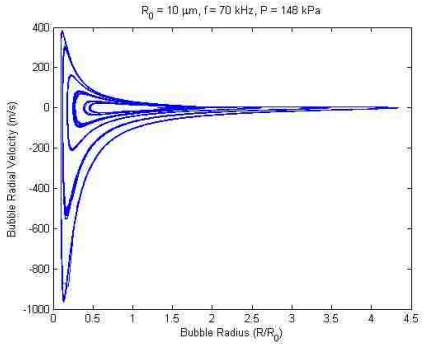


(a) Orbit, 70 kHz, MI = 0.56

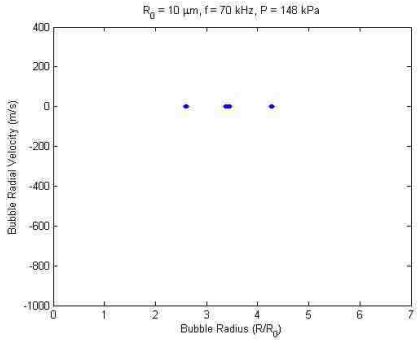


(b) Poincaré, 70 kHz, MI = 0.56

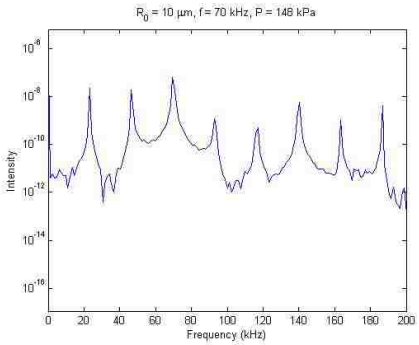


(c) Spectrum, 70 kHz, MI = 0.56

**Figure 6.15:** For a single 10 $\mu$m bubble at 70 kHz applied pressure and at a MI = 0.56: (a) trajectory in state space projection, (b) Poincaré section plot, and (c) frequency spectrum.

The frequency spectrum (Fig. 6.15(c)) reveals sharp peaks at $f/3 = 23.3$ and $2f/3 = 46.6$ with a small shoulder all that remains of the subharmonic signal. This suggests the existence of periodic points of period three in discrete space, confirmed

by the Poincaré cross-section in Figure 6.15(b). As explained in the previous section, according to Sarkovskii's ordering, the existence of periodic points of period three implies the existence of periodic points of all periods, even if a numerical algorithm remains blind to them.

This chaotic pattern continues up to and past MI = 0.70, with a strange attractor creating oscillations of all periods along with windows of periodic points of period three. An example of the chaos encountered at these values is given Figure 6.16, where A = 153 kPa and MI = 0.58.

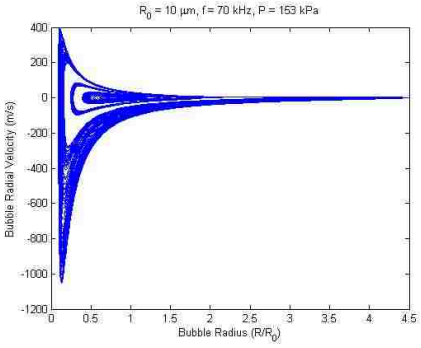


(a) Orbit, 70 kHz, MI = 0.58

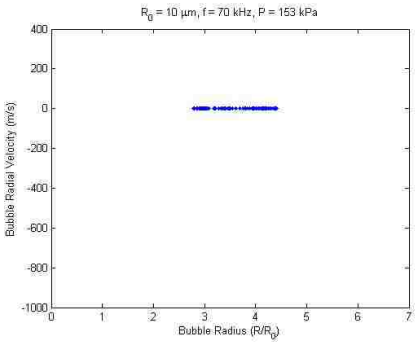


(b) Poincaré, 70 kHz, MI = 0.58

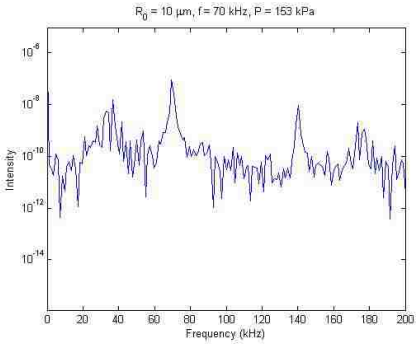


(c) Spectrum, 70 kHz, MI = 0.58

**Figure 6.16:** For a single 10 $\mu$m bubble at 70 kHz applied pressure and at a MI = 0.58: (a) trajectory in state space projection, (b) Poincaré section plot, and (c) frequency spectrum.

As expected, the projected orbit (Fig. 6.16(a)) retains the basic shape seen before with the addition of self-similar windings and twists within it. The Poincaré

plot (Fig. 6.16(b)) tells little, perhaps due to the time interval of integration not allowing for a full picture to form. The frequency spectrum confirms the chaotic nature of the system at this pressure value, Figure 6.16(c) shows an increase in background noise, indicative of the presence of all frequencies.

The preceding results for a 10 $\mu$m bubble driven at 70 kHz stand out for their difference from those at 500 kHz. The bubble oscillations are not as uniform as those seen at the higher frequency and follow a sequence of intermittent routes to and back from chaos as the pressure is changed. At MI $\approx 0.32$ the bubble undergoes a period-doubling bifurcation and then at about MI $= 0.35$ either a single or a number of saddle-node bifurcations push the system from stable to chaotic oscillations. Immediately prior to this bifurcation, however, the double-perid seems to disappear as the two periodic points slowly coalesce, though this may be a signature of the intermittent nature of the route to chaos. The strange attractor disappears at about MI $= 0.43$, where a stable limit cycle is created only to period-double again at about MI $= 0.50$ and eventually enter a new chaotic regime intermittently. This chaotic regime then persists up to at least MI $= 0.70$.

## 6.4 Discussion

The dynamics of an oscillating bubble under the action of ultrasound are markedly different between 70 and 500 kHz. This was expected since the system of equations of motion of bubble dynamics is a well known chaotic dynamical system. But just how different and how does this relate to drug release from micelles? We summarize the findings of this chapter for each frequency in what is called a *bifurcation diagram.*

In the realm of discrete dynamical systems, a bifurcation diagram simply plots the periodic points (including fixed points, of course) of a map against a control parameter. Thus, they contain the entire dynamic history of the system for the parameter of interest. For the system of differential equations studied in this research, the link between the continuous and discrete is the Poincaré plot, explained in detail previously. Even if we cannot find its explicit analytic form, the qualitative results

presented above allow us to create a rough sketch of the bifurcation diagrams. We choose the bubble radius given by the Poncaré map (after Parlitz *et al.* [67]) as the state variable for the bifurcation diagrams.

Figure 6.17 presents the bifurcation diagrams as a function of the mechanical index (MI) for 500 (Fig. 6.17(a)) and 70 kHz (Fig. 6.17(b)). These plots effectively summarize the results of the previous two sections.

Figure 6.17(a) shows the well-known pattern of the period-doubling route to chaos, especially due to its windows of stable period-three orbits (at about 0.50 and 0.68 in MI) and its covering of a large interval of $R/R_0$ values in the chaotic regime. This contrasts with Figure 6.17(b)'s intermittent route to, back from, then back to chaos. Not only does period-doubling never happen past points of period two, but the chaotic regime intervals are much narrower (and seem to follow an increasing $R/R_0$ pattern) than those found at 500 kHz.

The seemingly discontinuous jumps in $R/R_0$ as the MI increases are unexpected. This happens at precisely the second period-doubling (MI $\approx$ 0.33) for 500 kHz and at the start and end of the first chaotic regime (MI $\approx$ 0.35 and 0.43) for 70 kHz. There are two possible explanations for this phenomenon. Either it is a result of the dynamic structure of the oscillator or it is a numerical artifact arising from the integration algorithm used by MATLAB. If the latter is true, the qualitative differences in bubble behavior may still yield valid arguments for comparison between frequencies.

If the discontinuities are a characteristic of the system structure, they may arise out of saddle-node bifurcations. As explained before, saddle-node bifurcations govern the creation and destruction of limit cycles (through stability of orbits). Discontinuous jumps in bifurcation diagrams are precisely the destruction of a stable limit cycle and the creation of a new stable one (in this case, one that crosses the surface of section $S$ at a larger radius). Lauterborn explains this type of bifurcation to some length [46] and presents bifurcation diagrams with similar (seemingly) discontinuous behavior for the bubble oscillator itself [46, 67], using the driving frequency as the control parameter rather than the pressure amplitude as in this work. We established that

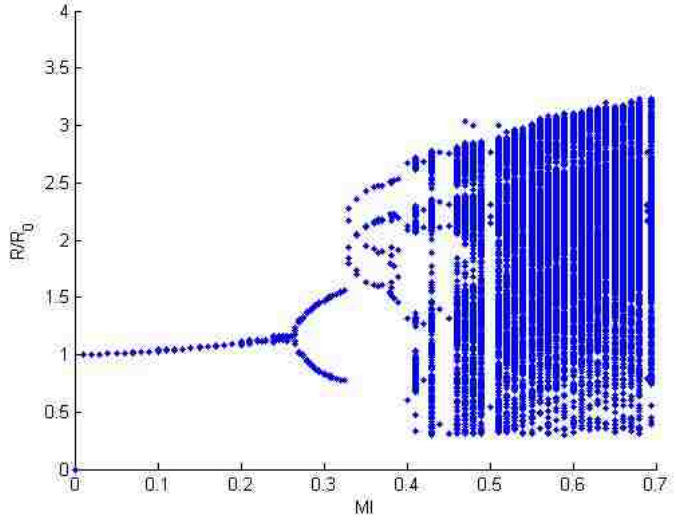


(a) BIfurcation Diagram for insonation $f = 500$ kHz

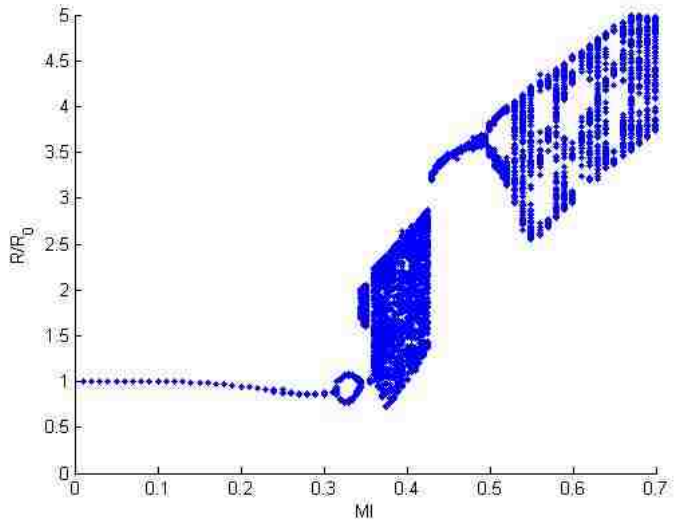


(b) BIfurcation Diagram for insonation at $f = 70$ kHz

**Figure 6.17:** Bifurcation diagrams as a function of applied pressure for a 10 $\mu$m bubble at: (a) $f = 500$ kHz and (b) $f = 70$ kHz.

the route to chaos at 70 kHz is intermittent in the previous section, which route proceeds through a single or a series of saddle-node bifurcations. It is therefore reasonable to consider that such a bifurcation created the discontinuities at 70 kHz.

The mystery is why a saddle-node bifurcation would occur in the middle of a period-doubling route to chaos (at 500 kHz). To confirm that this is a true saddle

node bifurcation, the hyperbolicity of the system of differential equations must be studied in detail in the neighborhood of the bifurcation using the analytical tools of chaos dynamics. In the present study we are not concerned with the details of this phenomenon, but solely with gaining a rough idea of the qualitative behavior of the bubble and it is thus not necessary to delve any deeper into this. This is nevertheless a future area of research to explore.

The bifurcation diagrams in Figure 6.17 elegantly illustrate the chaotic nature of the bubble oscillator, in particular, the chaotic map that is created when one moves to discrete space via the Poincaré plot. In order to interpret this further, we provide a basic definition of a chaotic map (from Devaney [14]).

**Definition 5.** Let $V$ be a set. Then $f : V \to V$ is said to be chaotic on $V$ if

1. $f$ has sensitive dependence on initial conditions
2. $f$ is topologically transitive
3. periodic points are dense in $V$

Briefly, the first condition is present if for any $x \in V$, there exist points arbitrarily close to $x$ which eventually separate from $x$ by at least some $\delta > 0$ under iteration of $f$. The second condition means that a particular map has points which eventually move under iteration from one arbitrarily small neighborhood to any other. Finally, the third condition states that for any $x \in V$, any neighborhood of $x$ contains at least one periodic point.

It can be shown that if $V \in \mathbb{R}$, then the second condition implies the rest. In any topological space, the second and third condition imply the first. No rigorous attempt to prove that the Poincaré map of the bubble oscillator is chaotic will be attempted here (especially since we do not know what it is analytically) but the last two conditions are easy to see from the preceding results. Topological transitivity can be seen by the "smearing" of points in the Poincaré cross-section as points are taken, under iteration, from one neighborhood to another. We have already shown that the system exhibits periodic points of all periods (necessarily an infinite number

of points and periods) and the bifurcation diagrams show that any interval in the strange attractor regime will contain periodic points. The discrete Poincaré map is therefore chaotic.

Given that all periods (i.e., frequencies) are present at the onset of chaos, we can then directly relate the onset of chaos (the appearance of a strange attractor) to the shift in baseline seen in the experiments, which means that background noise does not necessarily imply a collapse event. The literature lacks a well-defined criterion to identify a collapse event out of the equations of bubble dynamics. The approaches differ by author and include defining the moment of collapse as the point at which the bubble contents reach a temperature of 5000 K [3] and when radial oscillations show "sharp peaks" in the direction of small values of the radius [67]. Using the criterion of bubble wall velocity exceeding the speed of sound in air (explained in the previous section) to identify collapse is sufficient for our qualitative purposes and reveals that the bubble starts collapsing at around a mechanical index of 0.40 for 70 kHz but does not occur until about 0.70 for 500 kHz. In any case, we can see that collapse is approached by the increasingly violent behavior of the bubble (particularly in its inward movement) as the applied pressure increases, similar to its approach to chaos.

Having thus established the connection between the information presented by the bifurcation diagrams and the physical phenomena they represent, we can succinctly state the fundamental difference between bubble oscillations at 70 and 500 kHz: the bubble follows different routes to chaos, leading to contrasting behavior at collapse. Interpreting the meaning of this statement proves rather difficult, however, but raises a number of interesting questions. The first, of course, is: what do we mean physically when we speak of a route (or path) to chaos?

The period-doubling route to chaos contrasts with the intermittent one in that it appears to be more gradual and deliberate than the intermittent movement between stable oscillations and sudden and erratic chaos. A difference reported by Lauterborn [46] is the existence of hysteresis under the intermittent route to chaos (a testable phenomenon for future research). Additionally, the oscillations themselves appear to be quite different (see the orbit diagrams in the previous two sections), with oscilla-

tions at 70 kHz more uneven and unstable than at 500 kHz (a possible consequence of resonance, as argued earlier). It is possible that the forces that alter the structure of a micelle are produced only under the type of "quasi-stable" subharmonic oscillations seen at 70 kHz and that the transient and gradual period-doublings at 500 kHz are insufficient for this effect. A future experiment to test this would be to measure the forces, temperatures, and pressures generated locally under both types of routes to chaos and compare them.

It was hypothesized earlier that bubble resonance played the defining role in the drastically different type of oscillations leading to chaos that were seen at the two frequencies. This provides future avenues of research rich in possibilities. Looking at the diagrams in Figure 6.17 one must remember that they are but slices (i.e., projections) of a highly complex multi-dimensional space. If we let the axis perpendicular to the plane shown represent the equilibrium bubble size $R_0$ and move along it, the resulting surface will reveal the effect of resonance the we have discussed. For example, the small period-doubling window in Figure 6.17(b) ($0.32 \leq \mathrm{MI} < 0.35$) could very likely change in radius as $R_0$ changes and affect the resulting route to chaos. Comparison of these predictions with experiments in which the bubble sizes present are carefully controlled would be the next natural step.

These routes to chaos must also be shown to occur experimentally. Period-doubling was not seen in the experiments conducted at 500 kHz, although the series of period-doublings could have been so fast as to avoid detection by the experimental system. Parlitz [66] recently presented a method to locate period-doubling and saddle-node bifurcations in experimental systems. Using these tools the presence of both routes to chaos could be confirmed for the experimental system directly. Conversely, an analytical approach to the problem will yield the conditions necessary to create the single (or series of) saddle-node bifurcation needed at 500 kHz for an intermittent route to chaos like the one witnessed at 70 kHz. In this case the tools of bifurcation theory (in particular, catastrophe theory) could be used to figure out under which parameter values a fold in the geometry of parameter space could be reproduced at

500 kHz. Recorded drug release under such conditions would finally confirm that, indeed, the route to chaos followed by the bubbles is directly responsible for release.

Ultimately, drug release correlated with the subharmonic signal and not bubble collapse itself. This is why it is pertinent to focus on the long-term dynamic differences between frequencies and not exclusively on the moment of collapse. It is the subharmonic that still holds the answer. That the subharmonic signal should be intermittent at 70 kHz seems to be confirmed by the three outliers seen in Figure 5.6 and explained earlier. It is possible that the experimental setup used for 70 kHz (a water bath) created (through hysteresis and/or a distribution of bubble sizes) a wider window of intermittent subharmonic/chaotic oscillations than the bifurcation diagram predicts and that these "quasi-stable" oscillations died off eventually [46], characterized by the leveling off in percent drug release seen in Figure 5.4.

FInally, all of these findings challenge the validity of the original questions asked in Chapter 1. Can we still say (with apologies to Gertrude Stein) that a collapse is a collapse is a collapse? Or, more to the point, that a subharmonic is a subharmonic is a subharmonic? This research has shown two seemingly baffling conclusions: (1) drug release correlates with the subharmonic signal at 70 kHz but not at 500 kHz (where it is not even experimentally detectable though theoretically predictable) and (2) bubble collapse is not sufficient for drug release at either frequency. Such apparent paradoxes only serve to add to the confusion already present in the long-ongoing stable vs. collapse cavitation debate. Actually, however, what these findings reveal is that we have been asking the wrong questions all along. The chaotic nature of bubble dynamics shows that our physical interpretation of bubble oscillations cannot possibly remain within the oversimplified rubric of "stable" or "collapse." Indeed, our definition and categorization of cavitation must be updated to include cases analogous to all the dynamic states present in this complex dynamical system, including, but not limited to, the two distinct routes to chaos here discussed. The definition of mechanical index may have to be reevaluated similarly as well. Admittedly, in order to fully define all types of cavitation, parameter space must be explored fully (a herculean task, to say the least). In the present case, it can at least be said that drug

release requires and correlates with a type of "intermittent subharmonic" but not with the "cascade subharmonic" associated with the period-doubling route to chaos.

# Chapter 7

# Conclusions and Recommendations

## 7.1 Conclusions

Sequestration of harmful chemotherapeutic agents and their subsequent controlled release at the tumor site promises to be a more humane alternative to the present practice in cancer treatment. The use of Pluronic$^{TM}$ and Pluronic$^{TM}$-derived cross-linked micelles as drug carriers together with low-frequency ultrasound application as a release trigger has been previously shown to achieve this end both *in vitro* and *in vivo*. The question remained as to the viability of the system at higher frequencies, its potential to be focused and to operate at conditions closer to those in wide use in the world of ultrasound diagnostics. Additionally, the possible use of novel stabilized polymeric micelles as carriers also needed to be addressed. In essence, the question reduced itself to the role of the phenomenon known as cavitation in drug release.

The foregoing results and accompanying analysis demonstrate that ultrasound-induced drug release from polymeric micelles at 70 kHz is, in general, independent of drug carrier (stabilized or not) and temperature, which solely affect the absolute amount of drug released but not the mechanism itself. The existence of a drug release threshold (between 0.35 and 0.40 in mechanical index) suggested that cavitation (generally defined) was responsible for drug release. Acoustic spectra confirmed this suspicion as subharmonic intensity correlates faithfully with drug release, the signal appearing at the same time as the onset of release. Bubble collapse occurred before drug release was detected, implying that the subharmonic oscillations involved in drug release are independent of the violent collapse associated with acoustic signatures such as the increase in background noise. In the same vein, no drug release (or

subharmonic signal) was detected at 500 kHz despite evidence of bubble collapse in the form radical generation and baseline shift in the acoustic spectrum.

A mathematical model investigation into the differences between bubble behavior at 70 and 500 kHz revealed that the dynamics of bubble oscillations are fundamentally different. For a single 10 $\mu$m bubble, oscillations under 70 kHz were more irregular and unstable than those at 500 kHz, most likely due to the bubble's resonance frequency (330 kHz) being closer to the higher than the lower frequency. This difference was ultimately reflected in the choice of routes to chaos by the bubble. It was found that at 70 kHz the bubble follows an intermittent route to chaos (with a subharmonic signal appearing at about 0.32 in mechanical index) while, at 500 kHz, the bubble followed the more well-known period-doubling route to chaos (the subharmonic appearing around 0.275 in mechanical index).

Given that (1) bubble activity is directly correlated with drug release at 70 kHz, (2) there is no change in fluorescence suggesting no drug release at 500 kHz, and (3) bubble activity is dynamically different between the two frequencies, it was concluded that "intermittent subharmonic" oscillations at 70 kHz were responsible for change in fluorescence, and possibly drug release (as opposed to the "cascade subharmonic" oscillations seen at 500 kHz). Hence, if drug release is to be achieved at higher frequencies, the parameters must be such that this type of intermittent cavitation will be produced.

The contributions to the body of research in this subject that were presented in this thesis are as follows:

1. Establishing that ultrasonic drug release from Pluronic$^{TM}$ micelles as indicated by a decrease in Dox fluorescence is not possible at 500 kHz under the system parameters as presently constituted.

2. Confirmation that bubble dynamic activity (cavitation) is, at the very least, a major factor in drug release at 70 kHz.

3. Exploration of the effect of carrier stabilization and temperature in drug release: both influence amount of drug released yet the mechanism apparently remains the same.

4. Finding that drug release at 70 kHz correlates with the subharmonic signal of the acoustic spectrum.

5. Establishing the main dynamic difference in bubble oscillations between 70 and 500 kHz: an intermittent and a period-doubling route to chaos, respectively.

## 7.2 Recommendations and Future Work

This research does not say that ultrasonic drug release from micelles is not possible at high frequencies. It merely showed that under the experimental conditions used, no change in Dox fluorescence is detected at 500 kHz. Mathematical modeling revealed key aspects of the dynamic behavior of bubbles at 70 kHz (where release is seen) that are deemed necessary for release at other (including higher) frequencies. The main recommendation is to conduct experiments at 500 kHz (and possibly higher frequencies) under conditions that reproduce the intermittent cavitation seen at 70 kHz. A controlled distribution of bubble size is critical for these experiments. Such experiments will confirm that it is this type of cavitation and not a simple collapse that is responsible for drug release and provide the conditions to extend this treatment into eventual clinical trials.

A refinement of the laser detection system is suggested in order to make sure that the fluorescence changes measured actually correspond to drug release and not to some artifact created by clouds of bubbles created and induced into motion by the applied ultrasound. An assay-type experimental setup where a molecule that preferentially binds to Dox is included in the present system would achieve this end. Also, experiments should be conducted at 70 kHz where the driving pressure signal is modified as well as the geometry of the container is altered in order to "clean up" the signal presently used (by eliminating standing waves, for example) and thereby conduct experiments closer to the conditions modeled.

Investigation and confirmation of the suggested different types of cavitation is an important future work related to this research. First, a stronger characterization of the cavitation phenomena described in this study is needed, including mechanical and thermodynamic (by measuring the forces, temperatures, pressures, etc. created during the routes to chaos investigated). Second, these routes to chaos must be identified experimentally in order to confirm their existence in the system studied. Third, a more expansive and exhaustive mathematical analysis of the bubble oscillator system must be carried out in order to characterize its dynamic behavior over the entire parameter space. Finally, these results must be synthesized in order to create a more accurate and descriptive definition and characterization of cavitation activity.

# Appendix A

## 500 kHz Transducer Calibration

The voltage at the spot of highest intensity in the acoustic chamber ($(x, y, z) = (0.3, 0.3, 0.3)$ in. on the calipers) was measured using the hydrophone while the voltage supplied to the transducer was varied using a signal generator. Figure A.1 shows that the relationship is linear.

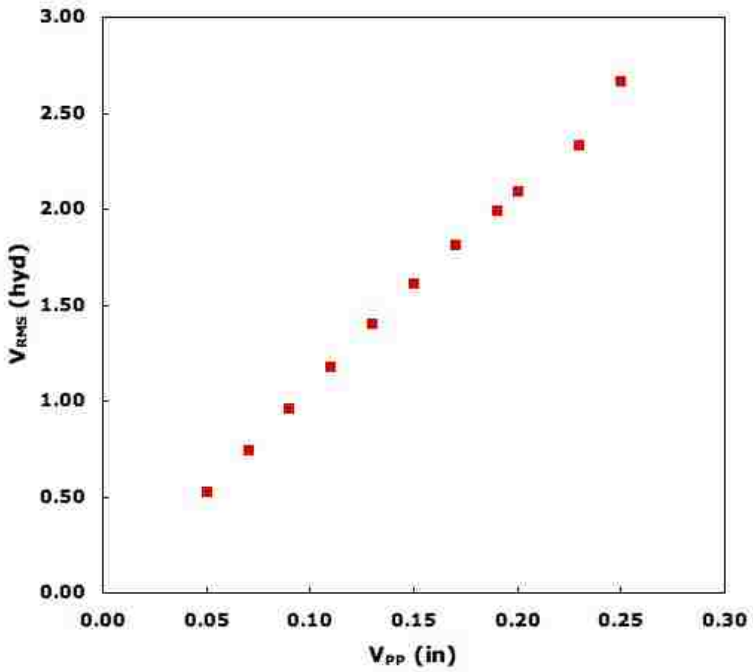


**Figure A.1:** $V_{RMS}$ from hydrophone vs. $V_{PP}$ from signal generator.

A least-squares fit ($R^2 = 0.9974$) of the data above gave the relationship between the voltage supplied through the signal generator ($V_{PP}^{in}$) and the voltage read by the hydrophone at the hotspot ($V_{RMS}^{hyd}$) as:

$$V_{RMS}^{hyd} = 10.368\ V_{PP}^{in} + 0.0292\ V. \tag{A.1}$$

# Appendix B

# MATLAB Code

### B.1 Keller-Miksis Equation

This function contains the bubble dynamics equations of the Keller-Miksis-Parlitz model for 500 kHz. It can easily be adapted to 70 kHz as well as into any other bubble model by simply changing the appropriate terms in the line starting with vdot(1).

```
%%%%%%%%%%%%%%%%%%%%%%%%%%%%%%%%%%%%%%%%%%%
%                                         %
% keller_laut_500k.m          Mario Diaz  %
%-Function file containing bubble dynamics %
%   equations for Keller-Lauterborn model %
%-Use with bubble500.m to solve           %
%-Takes initial conditions as arguments   %
%-All SI units                            %
%                                         %
%%%%%%%%%%%%%%%%%%%%%%%%%%%%%%%%%%%%%%%%%%%

function vdot=keller_laut_500k (t,v)

%---------------%
%   Constants   %
%---------------%

R0 = 10e-6;                  %Equilibrium radius
```

```
f = 500000;                 %Frequency
A = xedni(f, 0.71)*10^3;%Pressure amplitude for given MI

S = .073;                   %Surface tension
muL = 0.001;                %Dynamic viscosity
rhoL = 998;                 %Density
vL = 1.0e-6;                %Kinematic viscosity
c = 1500;                   %Speed of sound in water

pvtinf = 2.34e3;            %Vapor pressure
pinf0 = 1.01325e5;          %Static pressure

k = 1.4;                    %Heat capacity ratio


%--------------------%
%   Eq. System     %
%--------------------%
    %d[u r theta]
vdot(1) = ( (-0.5*(v(1))^2)*(3-(v(1)/c))...
    + (1+(1-3*k)*(v(1)/c))*(((pinf0-pvtinf)/rhoL)...
    +(2*S/(rhoL*R0)))*(R0/v(2))^(3*k)...
    - (2*S/(rhoL*v(2))) - (4*vL*v(1)/v(2))-...
    (1+(v(1)/c))*((pinf0-pvtinf+A*sin(2*pi*mod(v(3),1)))/rhoL)...
    - v(2)*cos(2*pi*mod(v(3),1))*(2*pi*f*A/(rhoL*c)))...
    *((1-(v(1)/c))*v(2) + 4*vL/c)^(-1);
vdot(2) = v(1);
vdot(3) = f;

vdot = vdot.';              %Make into column vector
```

### B.2 Solution of Bubble Dynamics Equations

This m-file solves the equations above and plots the diagrams seen in Chapter 6 for 500 kHz. It can be changed to solve for 70 kHz. Any bubble model can be used by using the appropriate function title in the ode45 call.

```
%%%%%%%%%%%%%%%%%%%%%%%%%%%%%%%%%%%%%%%%%%
%                                        %
% bubble500.m           Mario Diaz       %
%-Solves bubble dynamics equations       %
%-Generates phase diagrams, FT spectrum  %
%   and Poincare plots                   %
%                                        %
%%%%%%%%%%%%%%%%%%%%%%%%%%%%%%%%%%%%%%%%%%


%------------%
%  Timespan  %
%------------%
t0 = 0;
tf = 0.0004;      %end time (in seconds)

%create two new time vectors:
    %fixed time step (for FT)
tspan = t0:0.0000002:tf;
    %step same as applied period (for Poincare)
tspanp = t0:(1/500000):200*(1/500000);


%--------------------%
% Initial Conditions %
%--------------------%
    %[u R theta]
```

```
X0 = [0  10e-6  0];
    %equilibrium radius for normalization
R0 = 10e-6;

%-----------------------------------------%
% Solve equations for each time vector %
%-----------------------------------------%
    %data for FT
[t,X] = ode45('keller_laut_500k',tspan,X0);
    %data for phase diagrams
[tg,Xg] = ode45('keller_laut_500k',[t0 tf], X0);
    %data for Poincare plot
[tp,Xp] = ode45('keller_laut_500k',tspanp, X0);

%Create vectors for each solution:
r = X(:,2);
rnorm = r/R0;    %normalize
rdot = X(:,1);

theta = mod(Xg(:,3),1);

rg = Xg(:,2);
rnormg = rg/R0; %normalize
rdotg = Xg(:,1);

rp = Xp(:,2);
rnormp = rp/R0; %normalize
rdotp = Xp(:,1);

%Convert to micrometers and microseconds
```

```
rmicrons = r*1000000;
tmsecs = t*1000000;

rmicronsg = rg*1000000;
tmsecsg = tg*1000000;

rmicronsp = rp*1000000;
tmsecsp = tp*1000000;

%------------------------%
%  Fourier Transform  %
%------------------------%
Y = fft(X(:,2),4096);
Pyy = Y.* conj(Y) / 4086;
smplrate = 1 / 0.0000002;
f = smplrate*(0:2048)/4096;
    %y-axis limits for better plotting:
limit = Pyy(410)*6;          %normal plot
limitlog = Pyy(410)*100;     %log plot
freqkHz = f/1000;            %convert to kHz


%------------------------%
%   Generate Plots   %
%------------------------%
    %get pressure (kPa) for given mechanical index (MI)
kiloPress = xedni(500000, 0.71);
    %convert pressure into a string
press_string = ['P = ', num2str(kiloPress,4), ' kPa'];
```

```
%First figure plots radius and velocity vs. time
figure (1)
subplot(211)
plot(tmsecsg,rnormg)
% axis([250 300 0.5 1.5])   %adjust axes as needed
xlabel('Time (\mus)')
ylabel('Bubble Radius (R/R_0)')
title(['R_0 = 10 \mum, f = 500 kHz, ',press_string]);

subplot(212)
plot(tmsecsg,rdotg)
% axis([250 300 -10 10])    %adjust axes as needed
xlabel('Time (\mus)')
ylabel('Bubble Radial Velocity (m/s)')

%Plot phase diagram projection onto radius-velocity plane
figure(2)
plot(rnormg, rdotg);
xlabel('Bubble Radius (R/R_0)')
ylabel('Bubble Radial Velocity (m/s)')
title(['R_0 = 10 \mum, f = 500 kHz, ',press_string]);

%Plot complete solution in Euclidean space (not on torus)
figure(3)
plot3(rdotg,rnormg,theta);
title(['R_0 = 10 \mum, f = 500 kHz, ',press_string]);

%Plot Fourier Transform as given
figure(4)
plot(freqkHz, Pyy(1:2049));
```

```
axis([0 1100 0 limit])
xlabel('Frequency (kHz)')
ylabel('Intensity')
title(['R_0 = 10 \mum, f = 500 kHz, ',press_string]);

%Plot Fourier Transform on log plot
figure(5)
semilogy(freqkHz, Pyy(1:2049));
axis([0 1100 0 limitlog])
xlabel('Frequency (kHz)')
ylabel('Intensity')
title(['R_0 = 10 \mum, f = 500 kHz, ',press_string]);

%Plot Poincare cross-section
figure(6)
plot(rnormp,rdotp,'.');
axis([0 3.5 -400 300])
xlabel('Bubble Radius (R/R_0)')
ylabel('Bubble Radial Velocity (m/s)')
title(['R_0 = 10 \mum, f = 500 kHz, ',press_string]);
```

## B.3 Mechanical Index

Simple function that quickly returns an applied pressure from a mechanical index (MI) at any frequency.

```
%%%%%%%%%%%%%%%%%%%%%%%%%%%%%%%%%%%
%                                 %
% xedni.m         Mario Diaz      %
%-Gives pressure (in kPa)         %
%   for given MI                  %
%                                 %
%%%%%%%%%%%%%%%%%%%%%%%%%%%%%%%%%%%

function kiloPress = xedni(freq, MI)

    %convert to MHz:
freqMega = freq / 10^6;
    %definition of MI:
PressMega = MI * sqrt(freqMega);
    %convert to Pa:
Press = PressMega * 10^6;
    %convert to kPa:
kiloPress = Press / 10^3;
```

## Bibliography


[1] I. Akhatov, U. Parlitz, and W. Lauterborn. Pattern formation in acoustic cavitation. *Journal of the Acoustical Society of America*, 96(6):3627–3635, December 1994. 8, 44

[2] J. S. Allen, D. E. Kruse, P. A. Dayton, and K. W. Ferrara. Effect of coupled oscillations on microbubble behavior. *Journal of the Acoustical Society of America*, 114(3):1678–1690, September 2003. 30

[3] R. E. Apfel and C. K. Holland. Gauging the likelihood of cavitation from short-pulse, low-duty cycle diagnostic ultrasound. *Ultrasound in Medicine and Biology*, 17(2):179–185, 1991. 6, 23, 70

[4] A. A. Atchley and L. A. Crum. *Ultrasound: Its Chemical, Physical, and Biological Effects*, chapter Acoustic Cavitatin and Bubble Dynamics, pages 1–64. VCH Publishers, New York, 1988. 5

[5] S. B. Barnett. Thresholds for nonthermal bioeffects: Theoretical and experimental basis for a threshold index. *Ultrasound in Medicine and Biology*, 24(Supplement 1):S41–S49, 1998. 6, 23, 28

[6] S. B. Barnett, G. R. T. Haar, M. C. Ziskin, H.-D. Rott, F. A. Duck, and Z. Maeda. International recommendations and guidelines for the safe use of diagnostic ultrasound in medicine. *Ultrasound in Medicine and Biology*, 26(3):355–366, March 2000. 23

[7] E. Batrakova, T. Dorodnych, E. Klinsii, E. Kliushnenkova, O. Shemchukova, O. Goncharova, S. Arjakov, V. Alakhov, and A. Kabanov. Anthracyline antibiotics non-covalently incorporated into the block copolymer micelles: In vivo evaluation of anti-cancer activity. *British Journal of Cancer*, 74(10):1545–1552, November 1996. 4

[8] E. Batrakova, S. Lee, S. Li, A. Venne, V. Alakhov, and A. Kabanov. Fundamental relationships between the composition of pluronic block copolymers and their hypersensitization effect in mdr cancer cells. *Pharmaceutical Research*, 16(9):1373–1379, September 1999. 4

[9] C. E. Brennen. *Cavitation and Bubble Dynamics*. Oxford University Press, Inc., 200 Madison Avenue, New York, New York 10016, 1995. 2, 6, 8, 20, 29, 35, 40

[10] C. C. Church. Prediction of rectified diffusion during nonlinear bubble pulsations at biomedical frequencies. *Journal of the Acoustical Society of America*, 83(6):2210–2217, June 1988. 8, 9

[11] C. C. Church. A theoretical study of caviation generated by an extracorporeal shock wave lithotripter. *Journal of the Acoustical Society of America*, 86(1):215–227, 1989 1989. 8

[12] S. Daniels, D. Blondel, L. A. Crum, G. R. T. Haar, and M. Dyson. Ultrasonically induced gas bubble production in agar based gels: Part i, experimental investigation. *Ultrasound in Medicine and Biology*, 13(9):527–539, September 1987. 6

[13] M. Delius. Minimal static excess pressure minimises the effect of extracorporeal shock waves on cells and reduces it on gallstones. *Ultrasound in Medicine and Biology*, 23(4):611–617, 1997. 5

[14] R. L. Devaney. *An Introduction to Chaotic Dynamical Systems*. Studies In Nonlinearity. Westview Press, Boulder, Colorado, 2nd edition, 2003. 9, 42, 51, 53, 69

[15] Z. Ding and S. M. Gracewski. Response of constrained and unconstrained bubbles to lithotripter shock wave pulses. *Journal of the Acoustical Society of America*, 96(6):3636–3644, December 1994. 8

[16] E. C. Everbach, I. R. S. Makin, M. Azadniv, and R. S. Meltzer. Correlation of ultrasound-induced hemolysis with cavitation detector output in vitro. *Ultrasound in Medicine and Biology*, 23(4):619–624, 1997. 5

[17] H. G. Flynn and C. C. Church. Erratum: Transient pulsations of small gas bubbles in water [j. acoust. soc. am. 84, 985-998 (1988)]. *Journal of the Acoustical Society of America*, 84(5):1863–1876, November 1988. 6

[18] A. Gabizon, R. Catane, B. Uziely, B. Kaufman, T. Safra, R. Cohen, F. Martin, A. Huang, and Y. Barenholz. Prolonged circulation time and enhanced accumulation in malignant exudates of doxorubicin encapsulated in polyethylene-glycol coated liposomes. *Cancer Research*, 54(4):987–992, February 1994. 3

[19] D. F. Gaitan, L. A. Crum, C. C. Church, and R. A. Roy. Sonoluminescence and bubble dynamics for a single, stable, cavitation bubble. *Journal of the Acoustical Society of America*, 91(6):3168–3183, June 1992. 9

[20] T. Gudra and K. J. Opielinski. Applying spectrum analysis and cepstrum analysis to examine the cavitation threshold in water and in salt solution. *Ultrasonics*, 42:621–627, 2004. 6, 30

[21] C. R. Hill. Ultrasonic exposure thresholds for changes in cells and tissues. *The Journal of the Acoustical Society of America*, 52(2):667–672, 1972. 6, 28, 30

[22] M. W. Hirsch, S. Smale, and R. L. Devaney. *Differential equations, dynamical systems, and an introduction to chaos*, volume 60 of *Pure and Applied Mathematics*. Elsevier, San Diego, California, 2nd edition, 2004. 59

[23] C. K. Holland and R. E. Apfel. Thresholds for transient cavitation produced by pulsed ultrasound in a controlled nuclei environment. *Journal of the Acoustical Society of America*, 88(5):2059–2069, November 1990. 31, 35

[24] J. Holzfuss and W. Lauterborn. Liapunov exponents from a time series of acoustic chaos. *Physical Review A*, 39(4):2146–2152, February 1989. 9

[25] P. E. Huber, M. J. Mann, L. G. Melo, A. Ehsan, D. Kong, L. Zhang, M. Rezvani, P. Peschke, F. Jolesz, V. J. Dzau, and K. Hynynen. Focused ultrasound (hifu) induces localized enhancement of reporter gene expression in rabbit carotid artery. *Gene Therapy*, 10(18):1600–1607, September 2003. 6, 28

[26] G. Husseini, D. A. Christensen, N. Rapoport, and W. G. Pitt. Ultrasonic release of doxorubicin from pluronic p105 micelles stabilized with an interpenetrating network of n,n-diethylacrylamide. *Journal of Controlled Release*, 83(2):303–305, October 2002. 1, 4, 7

[27] G. Husseini, G. Myrup, W. Pitt, D. A. Christensen, and N. Rapoport. Factors affecting acoustically-triggered release of drugs from polymeric micelles. *Journal of Controlled Release*, 69(1):43–52, October 2000. 1, 4, 7, 13, 15, 16, 22, 25, 39

[28] G. Husseini, N. Rapoport, D. Christensen, J. Pruitt, and W. Pitt. Kinetics of ultrasonic release of doxorubicin from pluronic p105 micelles. *Colloids and Surfaces B: Biointerfaces*, 24(3-4):253–264, April 2002. 1, 4, 7, 29

[29] G. A. Husseini, R. I. El-Fayoumi, K. L. O'Neill, N. Y. Rapoport, and W. G. Pitt. Dna damage induced by micellar-delivered doxorubicin and ultrasound: comet assay study. *Cancer Letters*, 154(2):211–216, June 2000. 1, 7

[30] K. Hynynen, N. McDannold, H. Martin, F. A. Jolesz, and N. Vykhodtseva. The threshold for brain damage in rabbits induced by bursts of ultrasound in the presence of an ultrasound contrast agent (optison). *Ultrasound in Medicine and Biology*, 29(3):473–481, 2003. 6

[31] G. K. Johri, D. Singh, M. Johri, S. Saxena, and G. Iernetti. Measurement of the intensity of sonoluminescence, subharmonic generation and sound emission using pulsed ultrasonic technique. *Japanese Journal of Applied Physics*, 41(8):5329–5331, August 2002. 6, 30

[32] V. Kamath and A. Prosperetti. Numerical integration methods in gas-bubble dynamics. *Journal of the Acoustical Society of America*, 85(4):1538–1548, April 1989. 8, 9

[33] V. Kamath, A. Prosperetti, and F. Egolfopoulos. A theoretical study of sonolumiscence. *Journal of the Acoustical Society of America*, 94(1):248–260, July 1993. 8

[34] D. G. Kassan, A. M. Lynch, and M. J. Stiller. Physical enhancement of dermatologic drug delivery: Iontophoresis and phophoresis. *Journal of the American Academy of Dermatology*, 34(4):657–666, April 1996. 6

[35] K. Kataoka, G. S. Kwon, M. Yokoyama, T. Okano, and Y. Sakurai. Block-copolymer micelles as vehicles for drug delivery. *Journal of Controlled Release*, 24(1-3):119–132, May 1993. 3

[36] J. B. Keller and I. I. Kolodner. Damping of underwater explosion bubble oscillations. *Journal of Applied Physics*, 27(10):1152–1161, October 1956. 40

[37] J. B. Keller and M. Miksis. Bubble oscillations of large amplitude. *Journal of the Acoustical Society of America*, 68(2):628–633, August 1980. 40

[38] B.-R. Kim, J.-S. Jeon, and H.-Y. Kwak. Stability and selevtive bifurcation for a gas bubble oscillating under ultrasound. *Journal of the Physical Society of Japan*, 68(4):1197–1204, April 1999. 8, 9, 10

[39] J. B. Kruskal, S. N. Goldberg, and R. A. Kane. Novel in vivo use of conventional ultrasound to guide and enhance molecular delivery and uptake into solid tumors. *Radiology*, 221(419 Suppl S), November 2001. 6

[40] M. W. A. Kuijpers, D. van Eck, M. F. Kemmere, and J. T. F. Keurentjes. Cavitation-induced reactions in high-pressure carbon dioxide. *Science*, 298:1969–1971, December 2002. 6

[41] R. Langer. Biomaterials in drug delivery and tissue engineering: One laboratory's experience. *Accounts of Chemical Research*, 33(2):94–101, February 2000. 6

[42] W. Lauterborn. Numerical investigation of nonlinear oscillations of gas bubbles in liquids. *Journal of the Acoustical Society of America*, 59(2):283–293, February 1976. 9

[43] W. Lauterborn and E. Cramer. Subharmonic route to chaos observed in acoustics. *Physical Review Letters*, 47(20):1445–1448, November 1981. 9

[44] W. Lauterborn and A. Koch. Holographic observation of period-doubled and chaotic bubble oscillations in acoustic cavitation. *Physical Review A*, 35(4):1974–1976, February 1987. 9, 10

[45] W. Lauterborn and C.-D. Ohl. The peculiar dynamics of cavitation bubbles. *Applied Scientific Research*, 58(1-4):53–76, 1998. 9, 10

[46] W. Lauterborn and U. Parlitz. Methods of chaos physics and their applications to acoustics. *Journal of the Acoustical Society of America*, 84(6):1975–1993, December 1988. 9, 39, 44, 46, 52, 59, 63, 67, 70, 72

[47] W. Lauterborn and E. Suchla. Bifurcation superstructure in a model of acoustic turbulence. *Physical Review Letters*, 53(24):2304–2307, December 1984. 9

[48] T. Leighton. *The Acoustic Bubble*. Academic Press, London, 1997. 6, 11, 29, 30

[49] J. Liu, T. N. Lewis, and M. R. Prausnitz. Non-invasive assessment and control of ultrasound-mediated membrane permeabilization. *Pharmaceutical Research*, 15(6):918–924, 1998. 29, 30

[50] Y. Matsumoto and S. Yoshizawa. Behaviour of a bubble cluster in an ultrasound field. *International Journal for Numerical Methods in Fluids*, 47(6-7):591–601, February 2004. 8, 9, 44

[51] J. L. Mestas, P. Lenz, and D. Cathignol. Long-lasting stable cavitation. *Journal of the Acoustical Society of America*, 113(3):1426–1430, March 2003. 6, 30, 31

[52] D. L. Miller and R. M. Thomas. Thresholds for hemorrhages in mouse skin and intestine induced by lithotripter shock-waves. *Ultrasound in Medicine and Biology*, 21(2):249–257, 1995. 6

[53] S. Mitragotri, D. Blankschtein, and R. Langer. Ultrasound-mediated transdermal protein delivery. *Science*, 269(5225):850–853, August 1995. 6

[54] S. Mitragotri, D. Blankschtein, and R. Langer. Transdermal drug delivery using low-frequency sonophoresis. *Pharmaceutical Research*, 13(3):411–420, March 1996. 6

[55] S. Mitragotri, D. A. Edwards, D. Blankschtein, and R. Langer. Mechanistic study of ultrasonically-enhanced transdermal drug-delivery. *Journal of Pharmaceutical Sciences*, 84(6):697–706, June 1995. 6

[56] S. Mitragotri, J. Farrell, H. Tang, T. Terahara, J. Kost, and R. Langer. Determination of threshold energy dose for ultrasound-induced transdernal drug transport. *Journal of Controlled Release*, 63(1-2):41–52, January 2000. 6, 28

[57] S. Mitragotri and J. Kost. Low frequency sonophoresis: A noninvasive method of drug delivery and diagnostics. *Biotechnology Progress*, 16(3):488–492, May-June 2000. 6

[58] S. Mitragotri, D. Ray, J. Farrell, H. Tang, B. Yu, J. Kost, D. Blankschtein, and R. Langer. Synergistic effect of low-frequency ultrasound and sodium lauryl sulfate on transdermal transport. *Journal of Pharmaceutical Sciences*, 89(7):892–900, July 2000. 6

[59] K. I. Morton, G. R. T. Haar, I. J. Stratford, and C. R. Hill. Subharmonic emission as an indicator of ultrasonically-induced biological damage. *Ultrasound in Medicine and Biology*, 9(6):629–633, 1983. 5

[60] N. Munshi, N. Rapoport, and W. Pitt. Ultrasonic activated drug delivery from pluronic p-105 micelles. *Cancer Letters*, 118(1):13–19, September 1997. 4

[61] J. L. Nelson, B. L. Roeder, J. C. Carmen, F. Roloff, and W. G. Pitt. Ultrasonically activated chemotherapeutic drug delivery in a rat model. *Cancer Research*, 62(24):7280–7283, December 2002. 1, 7

[62] E. A. Neppiras. Subharmonic and other low-frequency emission from bubbles in sound-irradiated liquids. *The Journal of the Acoustical Society of America*, 46(3):587–601, 1968. 6, 29, 30

[63] S. Ning, K. Macleod, R. Abra, A. Huang, and G. Hahn. Hyperthermia induces doxorubicin release from long-circulating liposomes and enhances their anti-tumor efficacy. *International Journal of Radiation Oncology Biology Physics*, 29(4):827–834, July 1994. 3

[64] W. L. Nyborg. Biological effects of ultrasound: Development of safety guidelines. part ii: General review. *Ultrasound in Medicine and Biology*, 27(3):301–333, March 2001. 5, 6, 8, 19, 28, 30, 55

[65] R. Omta. Oscillations of a cloud of bubbles of small and not so small amplitude. *Journal of the Acoustical Society of America*, 82(3):1018–1033, September 1987. 8, 44

[66] U. Parlitz. Robust method for experimental bifurcation analysis. *International Journal of Bifurcation and Chaos*, 12(8):1909–1913, 2002. 71

[67] U. Parlitz, V. Englisch, C. Scheffczyk, and W. Lauterborn. Bifurcation structure of bubble oscillators. *Journal of the Acoustical Society of America*, 88(2):1061–1077, August 1990. 9, 10, 39, 42, 43, 44, 46, 52, 67, 70

[68] A. Phelps and T. Leighton. The subharmonic oscillations and combination-frequency subharmonic emissions from a resonant bubble: Their properties and generation mechanisms. *Acustica*, 83(1):59–66, January-February 1997. 9, 10, 30

[69] Y. Pomeau and P. Manneville. Intermittent transition to turbulence in dissipative dynamical systems. *Communications in Mathematical Physics*, 74(2):189–197, 1980. 59

[70] A. Prosperetti. Nonlinear oscillations of gas bubbles in liquids: transient solutions and the connection between subharmonic signal and cavitation. *Journal of the Acoustical Society of America*, 57(4):810–821, April 1975. 9

[71] A. Prosperetti. Subharmonics and ultraharmonics in the forced oscillations of weakly nonlinear systems. *American Journal of Physics*, 44(6):548–554, June 1976. 9

[72] A. Prosperetti. Application of the subharmonic threshold to the measurement of the damping of oscillating gas bubbles. *Journal of the Acoustical Society of America*, 61(1):11–16, January 1977. 9

[73] A. Prosperetti. Thermal effects and damping mechanisms in the forced radial oscillations of gas bubbles in liquids. *Journal of the Acoustical Society of America*, 61(1):17–27, January 1977. 8

[74] A. Prosperetti. A generalization of the rayleigh-plesset equation of bubble dynamics. *Physics of Fluids*, 25(3):409–410, March 1982. 8, 9

[75] A. Prosperetti, L. A. Crum, and K. W. Commander. Nonlinear bubble dynamics. *Journal of the Acoustical Society of America*, 83(2):502–514, February 1988. 8, 9

[76] J. Pruitt. *Stabilization of Pluronic P-105 for Targeted Nanoparticle Drug Delivery*. Ph.d. dissertation, Brigham Young University, Provo, Utah, 2001. 4

[77] J. Pruitt, G. Husseini, N. Rapoport, and W. G. Pitt. Stabilization of pluronic p-105 micelles with an interpenetrating network of n,n-diethylacrylamide. *Macromolecules*, 33(25):9306–9309, December 2000. 1, 4, 15

[78] J. D. Pruitt and W. G. Pitt. Sequestration and ultrasound-induced release of doxorubicin from stabilized pluronic p105 micelles. *Drug Delivery*, 9(4):253–258, October 2002. 7

[79] N. Rapoport. Stabilization and activation of pluronic micelles for tumor-targeted drug delivery. *Colloids and Surfaces B: Biointerfaces*, 16(1-4):93–111, November 1999. 3

[80] N. Rapoport, A. I. Smirnov, A. Timoshin, A. M. Pratt, and W. G. Pitt. Factors affecting the permeability of pseudomonas aeruginosa cell walls toward lipophillic compounds: Effects of ultrasound and cell age. *Archives of Biochemistry and Biophysics*, 344(1):114–124, August 1997. 6, 30

[81] J. Rooney. Hemolysis near an ultrasonically pulsating gas bubble. *Science*, 169:869–871, 1970. 29

[82] A. H. Saad and A. R. Williams. Effeects of therapeutic ultrasound on clearance rate of blood borne colloidal particles in vivo. *British Journal of Cancer*, 45((Suppl. V)):202–205, 1982. 6

[83] K. Saito, K. Miyake, P. L. McNeil, K. Kato, K. Yago, and N. Sugai. Plasma membrane disruption underlies injury of the corneal endothelium by ultrasound. *Experimental Eye Research*, 68(4):431–437, April 1999. 6

[84] L. Samek. A multiscale analysis of nonlinear oscillations of gas bubbles in liquids. *Journal of the Acoustical Society of America*, 81(3):632–637, March 1987. 9

[85] W. T. Shi, F. Forsberg, A. Tornes, J. Østensen, and B. B. Goldberg. Destruction of contrast microbubbles and the association with inertial cavitation. *Ultrasound in Medicine and Biology*, 26(6):1009–1019, 2000. 31

[86] S. H. Strogatz. *Nonlinear Dynamics and Chaos*. Westview Press, 1994. 46, 59

[87] J. Sundaram, B. R. Mellein, and S. Mitragotri. An experimental and theoretical analysis of ultrasound-induced permeabilization of cells membranes. *Biophysical Journal*, 84(5):3087–3101, May 2003. 6, 29, 30

[88] K. Tachibana and S. Tachibana. Albumin microbubble echo-contrast material as an enhancer for ultrasound accelerated thrombolysis. *Circulation*, 92(5):1148–1150, September 1995. 6

[89] K. Tachibana, T. Uchida, K. Ogawa, N. Yamashita, and K. Tamura. Induction of cell-membrane porosity by ultrasound. *Lancet*, 353(9162):1409, April 1999. 6

[90] A. Tezel, A. Sens, J. Tuchscherer, and S. Mitragotri. Frequency dependence of sonophoresis. *Pharmaceutical Research*, 18(12):1694–1700, December 2001. 6, 28, 29

[91] E. Unger, R. McCreery, R. Sweitzer, V. Caldwell, and Y. Wu. Acoustically active lipospheres containing paclitaxel: a new therapeutic ultrasound contrast agent. *Investigative Radiology*, 33(12):886–892, December 1998. 3

[92] R. J. Urick. *Principles of Underwater Sound*. McGraw-Hill Book Company, San Francisco, 3rd edition, 1983. 6

[93] A. Venne, S. Li, R. Mandeville, A. Kabanov, and V. Alakhov. Hypersensitizing effect of pluronic l61 on cytotoxic activity, transport, and subcellular distribution of doxorubicin in multiple drug-resistant cells. *Cancer Research*, 56(16):3626–3629, August 1996. 4

[94] S. Vyas, R. Singh, and R. Asati. Liposomally encapsulated diclofenac for sonophoresis induced systemic delivery. *Journal of Microencapsulation*, 12(2):149–154, March-April 1995. 3

[95] R. G. Williams and W. G. Pitt. In vitro response of escherichia coli to antibiotics and ultrasound at various insonation intensities. *Journal of Biomaterials Applications*, 12(1):20–30, July 1997. 6

[96] X. Yang, R. A. Roy, and R. G. Holt. Bubble dynamics and size distributions during focused ultrasound insonation. *Journal of the Acoustical Society of America*, 116(6):3423–3431, December 2004. 9

[97] M. Yokoyama. *Advances in Polymeric Systems for Drug Delivery*, chapter Site Specific Drug Delivery Using Polymeric Carriers, pages 24–66. Gordon and Breach Science Publishers, Iverdon, Switzerland, 1994. 3

[98] Y. Zeng and W. Pitt. Poly(ethylene oxide)-b-poly(n-isopropylacrylamide) nanoparticles with cross-linked cores as drug carriers. *Journal of Biomaterials Science: Polymer Edition*, 16(3):371–380, 2005. 4, 15